

## Three-Dimensional Structure and Evolution of the Vertical Velocity and Divergence Fields in the MJO

ÁNGEL F. ADAMES AND JOHN M. WALLACE

*Department of Atmospheric Sciences, University of Washington, Seattle, Washington*

(Manuscript received 3 April 2014, in final form 26 August 2014)

### ABSTRACT

The features in the planetary-scale wind field that shape the MJO-related vertical velocity field are examined using the linear analysis protocol based on the daily global velocity potential field described in a companion paper, augmented by a compositing procedure that yields a more robust and concise description of the prevalent patterns over the Indo-Pacific warm pool sector ( $60^{\circ}\text{E}$ – $180^{\circ}$ ). The analysis elucidates the structural elements of the planetary-scale wind field that give rise to the characteristic “swallowtail” shape of the region of enhanced rainfall and the “bottom up” evolution of the vertical velocity profile from one with a shallow peak on the eastern end of the region of enhanced rainfall to one with an elevated peak on the western end. These distinctive features of the vertical velocity field in the MJO reflect the juxtaposition of deep overturning circulation cells in the equatorial plane and much shallower frictionally driven cells in the meridional plane to the east and west of the regions of enhanced rainfall. The zonal overturning circulations determine the pattern of  $\partial u / \partial x$  and the meridional overturning circulations determine the pattern of  $\partial v / \partial y$  in the divergence profiles. These features are at least qualitatively well represented by the Matsuno–Gill solution for the planetary wave response to a stationary equatorial heat source–sink dipole.

### 1. Introduction

In their Fig. 16, Madden and Julian (1972) describe a planetary-scale circulation consisting of a succession of eastward-propagating cells extending through the depth of the troposphere in quadrature with belts of enhanced and suppressed convection. The cells circumnavigate the equatorial belt over a period of  $\sim 40$  days but are most pronounced when they are passing over the Indo-Pacific warm pool. Inspired by Matsuno’s (1966) theoretical analysis of planetary waves on an equatorial beta plane, J. R. Holton<sup>1</sup> suggested that the cell to the east of the enhanced convection in the Madden–Julian oscillation (MJO) is associated with an equatorially trapped Kelvin wave response and the cell to the west with a Rossby wave response. If the equatorial heat source

is a dipole or is envisioned as varying sinusoidally with longitude as in Matsuno’s solution, the Kelvin and Rossby wave components of the solution are not as easily distinguished, but the same dynamical arguments apply because the solution for a dipole heat source can be obtained by superimposing solutions for the corresponding monopole heat sources. This linear equatorial planetary wave paradigm was augmented by Webster’s (1972) and Gill’s (1980) extension of Matsuno’s analysis to three dimensions. In their solution, the vertical structure of the circulation and geopotential height fields consist of what Gill termed as the “first internal baroclinic mode,” which is characterized by a phase reversal of the wind and geopotential height patterns between the upper and lower troposphere. The structure described in the aforementioned studies has served as the framework for many theoretical studies of the MJO.

Subsequent studies have revealed aspects of the MJO structure that are not explained in terms of the shallow-water wave solutions of Matsuno (1966) and Gill (1980). Observational studies by Sperber (2003) based on

<sup>1</sup>In a personal communication with R. A. Madden in 1971.

Denotes Open Access content.

*Corresponding author address:* Ángel F. Adames, Department of Atmospheric Sciences, University of Washington, 408 ATG Building Box 351640, Seattle, WA 98195-1640.  
E-mail: angelf88@atmos.washington.edu

reanalysis data and Myers and Waliser (2003) based on satellite data showed that the MJO-related divergence and vertical velocity fields exhibit a westward phase tilt with height in the equatorial plane. Wang (1988) and Wang and Rui (1990) theorized that boundary layer friction acting upon the low-level easterlies to the east of an equatorial heat source induces meridional confluence (negative  $\partial v / \partial y$ ), causing near-surface convergence there. By the same argument, the westerly low-level flow to the west of the heat source should be divergent. When this frictionally induced component is taken into account, the total divergence field should exhibit a westward tilt with height in the equatorial plane. Kiladis et al. (2005) hypothesized that a westward tilt in height in the divergence field over the equatorial belt should also be reflected in the cloud morphology, with predominantly shallow convection preceding episodes of enhanced deep convection and elevated stratiform convection following them. In support of this interpretation, they cited in situ cloud observations in the tropical western Pacific taken during the Tropical Ocean and Global Atmosphere Coupled Ocean–Atmosphere Response Experiment (TOGA COARE) field campaign (Johnson et al. 1999). Analysis of satellite data by Riley et al. (2011), Lau and Wu (2010), and Barnes and Houze (2013) and in situ sounding and radar data by Yoneyama et al. (2008), Katsumata et al. (2009), and Powell and Houze (2013) also support the notion of a systematic “bottom up” evolution of convective clouds during the MJO cycle.

Zhang and Ling (2012) further investigated the role of diabatic heating in shaping the structure and evolution of the MJO by analyzing the distribution of potential vorticity. In their study, they identified a horizontal structure in precipitation that resembles a “swallowtail” (their Fig. 6b). This signature consists of a narrow band of enhanced precipitation to the east of the region of maximum precipitation, which splits into two off-equatorial bands that diverge toward the west. The mechanisms that give rise to this distinctive signature, which has also appeared in observational studies such as Hendon and Salby (1994) and in theoretical studies such as Wang and Rui (1990), are not completely understood. Some studies have interpreted the structure as the direct result of the dynamics of equatorial Kelvin and Rossby waves (Wang and Rui 1990; Maloney and Hartmann 1998), while others (Zhang and Ling 2012) have argued that this structure does not contain a clear signature of either type of equatorially trapped wave.

In the companion paper Adames and Wallace (2014, hereafter AW1) we show that the three-dimensional structure of the MJO is influenced by the strong meridional and vertical shears in the background (i.e., zonally averaged) zonal wind field. The influence of the climatological-mean westerly jets on

the upper-tropospheric (100–300 hPa) structure of the MJO is emphasized in particular. The analysis in AW1 is largely based on the MJO-related zonal wind  $u$  and geopotential height ( $Z$ ) anomaly fields, which are shown to be dominated by a deep baroclinic modal structure with perturbations of opposing polarity above and below the 400-hPa level. In contrast, this study is largely focused on the temperature  $T$ , vertical velocity  $\omega$ , and divergence (Div) fields and the main findings pertain to the lower troposphere (500–1000 hPa). We will show that the leading mode in the  $T$  field is dominated by the same baroclinic modal structure as described in AW1. The  $\omega$  field exhibits a more complex vertical structure involving two orthogonal modes, which are simply related to patterns of divergence in the boundary layer (850–1000 hPa) and lower-free-tropospheric (500–850 hPa) wind fields. We will show that the frictional convergence in the equatorial Kelvin wave in combination with the equatorial Rossby wave signature gives rise to a distinctive three-dimensional structure in the  $\omega$  field that accounts for the bottom-up evolution described above as well as the characteristic swallowtail shape.

As in AW1, the results are based mainly on the Interim European Centre for Medium-Range Weather Forecasts (ECMWF) Re-Analysis (ERA-Interim) from 1979 to 2011. The fields of temperature, vertical velocity, and horizontal divergence have previously been shown to be well represented in ERA-Interim and are in close agreement with satellite observations (Tian et al. 2010). As in AW1, the MJO cycle is defined in terms of linear combinations of the two leading principal components (PCs) of daily-mean global fields of 850- minus 150-hPa velocity potential ( $\Delta\chi$ ).

The paper is structured as follows: The next section describes the datasets and methods of analysis. Section 3 describes the three-dimensional structure of the temperature, vertical velocity, and divergence fields in the MJO cycle as inferred from regression analysis. In Section 4, MJO-related variations in the vertical profiles of temperature and vertical velocity are illuminated by decomposing the respective fields into modes using the methodology described in section 4 of AW1. Section 5 documents the structure of the decomposed vertical velocity field in the context of lower-tropospheric divergence field, taking into account the contributions from the boundary layer and the free troposphere. Section 6 presents a summary and discussion of the results.

## 2. Data and methods

The data and methods used in this study are similar to those in AW1. The primary dataset is the  $1.5^\circ$  longitude  $\times$   $1.5^\circ$  latitude horizontal resolution, 0000 UTC

daily ERA-Interim fields (Dee et al. 2011) for the 33-yr time interval 1979–2011. The horizontal wind components ( $u$ ,  $v$ ) are used in this study as field variables and in calculating the velocity potential ( $\chi$ ) and divergence (Div) fields. Geopotential height  $Z$ , temperature  $T$ , and vertical velocity  $\omega$  are also used in this study along with outgoing longwave radiation (OLR) from National Oceanic and Atmospheric Administration (NOAA)'s polar-orbiting satellites (Liebmann and Smith 1996).

For each field in this study, the mean and first three harmonics of the annual cycle, based on the 1979–2011 reference period, are removed, and the running mean of the previous 120 days is subtracted out as in Lo and Hendon (2000). The regression patterns presented here are based on the equation

$$\mathbf{D} = \mathbf{SP}^T/N, \quad (1)$$

where  $\mathbf{S}$  is a two-dimensional matrix that represents a variable field  $S$ ,  $\mathbf{D}$  is its regression pattern with dimensional units,  $\hat{\mathbf{P}}$  is a standardized MJO index, and  $N$  is the sample size (days). Most of the patterns presented here are obtained by regressing fields upon MJO indices defined as linear combinations of the two leading PCs of daily-mean global fields of 850- minus 150-hPa velocity potential  $\Delta\chi$ . Justification for the use of these indices is presented in AW1. In the appendix of AW1 it is shown that results based on these indices are similar to those based on MJO indices used in other studies.

We make use of the modal decomposition described in section 4 of AW1, which can be interpreted in the following manner. Within a prescribed domain such as 10°S–10°N the three-dimensional structure of the variable  $\psi$  at a particular time could be decomposed into a series of EOFs, each consisting of a set of maps on pressure levels, and the corresponding PCs defining the amplitudes to be assigned to the patterns at each level. This operation is analogous to conventional EOF analysis with time replaced by pressure level. The dimension of the data matrix would be  $G \times L$ , where  $G$  is the number of grid points and  $L$  is the number of pressure levels. To obtain more representative modal structures, one might choose to incorporate the data for  $T$  different map times in the analysis, in which case the dimension of the data matrix would become  $TG \times L$ . Our analysis is performed in MJO subspace, so in place of maps at specific times we use regression maps for  $\psi$  upon PC1 and PC2 of  $\Delta\chi$ , so the dimension of the data matrix is  $2G \times L$ . In AW1, we performed this modal analysis using maximal covariance analysis (MCA) of the  $u$  field paired with the  $Z$  field. Here we use EOF analysis to decompose the  $T$  and the  $\omega$  fields independently. We have performed the analysis of  $u$  paired with  $Z$  and  $\omega$  paired with  $T$  and found the results to be similar.

In some of the figures in this paper, we will also make use of compositing in the longitude domain to smooth out regional features in the warm pool region so that that the planetary-scale structure in the equatorial fields becomes more clearly apparent. In this procedure we average maps or longitude–height sections for a sequence of adjacent MJO phases, zonally shifting each one so that the all the maxima in  $\Delta\chi$  come into alignment.

The results presented in this paper are based on data for all 12 calendar months. As in AW1, the contour intervals in the plots correspond roughly to the 95% confidence intervals based on a two-sided  $t$  test. Hence, the features represented by all contours except the zero contour can be considered to be statistically significant. The dynamical consistency of the results presented here and their close correspondence with results obtained in previous studies also attests to their statistical significance.

### 3. The MJO-related structure of temperature, vertical velocity, and divergence

To gain a global perspective on the MJO let us consider the distribution of root-mean-square (rms) amplitude of  $u$ ,  $Z$ ,  $T$ , and  $\omega$  in the meridional plane. As in AW1, the rms amplitude is defined as the square root of the sum of the squared amplitude of the anomalies in regression maps  $D$  based on PC1 and PC2 of  $\Delta\chi$ ,  $D_{\text{rms}} = [1/2(D_1^2 + D_2^2)^{1/2}]$ . The “phases” of the MJO cycle, which we will discuss later in this section, are all based on linear combinations of these two sets of regression patterns. Maps of rms amplitude were generated for each pressure level and zonally averaged to create the meridional cross section shown in Fig. 1. The top panel shows the structure of the MJO in the  $u$  and  $Z$  fields, as in Fig. 13 of AW1. The maximum amplitudes of these fields are observed in the upper troposphere. The equatorial variance maximum in  $Z$  at 125 hPa corresponds to the MJO's equatorial Kelvin wave, while the centers of action located  $\sim 28^\circ\text{N/S}$ , just equatorward of the climatological-mean jet streams (denoted by the blue W), correspond to what we have referred to in AW1 as the “flanking Rossby waves.” The perturbations in the  $T$  field (middle panel) that peak at 250 and 100 hPa are hydrostatically consistent with the  $Z$  signatures. The largest  $T$  anomalies occur in conjunction with the  $Z$  anomalies associated with the flanking Rossby waves and extend poleward to  $\sim 50^\circ\text{N}$  and  $50^\circ\text{S}$ , overlapping with extratropical height anomalies that extend down to the earth's surface. We will refer to these belts extending from  $\sim 25^\circ$  to  $50^\circ\text{N/S}$  as the “Rossby wave corridors.”

The corresponding distribution of  $\omega$ , shown in the bottom panel of Fig. 1, exhibits well defined maxima over the equator and within the Northern and Southern Hemisphere Rossby wave corridors. The extratropical

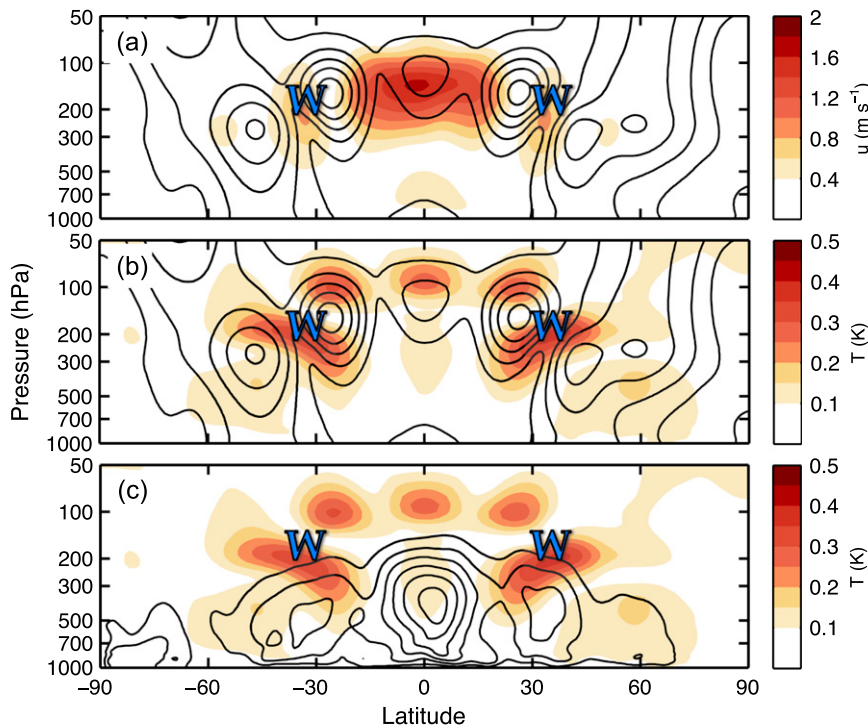


FIG. 1. RMS amplitude of MJO-related anomalies obtained from the regression patterns based on PC1 and PC2 of  $\Delta\chi$ . (a)  $Z$  (contoured) and  $u$  (shaded), (b)  $Z$  (contoured) and  $T$  (shaded), and (c)  $T$  (shaded) and  $\omega$  (contoured). Contour interval  $0.25 \text{ m s}^{-1}$  for  $u$ ,  $1.25 \text{ m}$  for  $Z$ ,  $0.1^\circ\text{C}$  for  $T$ , and  $1 \text{ hPa day}^{-1}$  for  $\omega$ . The locations of the climatological-mean westerly jets are depicted with a blue W. This and all subsequent figures are based on data for all calendar months.

maxima coincide with the latitudes of the strongest upper-tropospheric westerlies.

To document the meridional structure of  $T$  and  $\omega$  during different phases of the MJO, we show in the left panels of Fig. 2 a series of meridional cross sections describing the evolution of the MJO-related  $T$  and  $\omega$  fields at the longitude of the Maritime Continent, defined as the sector extending from  $120^\circ$  to  $150^\circ\text{E}$ . As in AW1, the five panels in each column correspond to snapshots at  $1/8$ -cycle intervals, spanning half the MJO cycle, the middle one coinciding with the peak of PC1 of  $\Delta\chi$ , which corresponds to the time when the MJO-related convection is passing eastward across the Maritime Continent, and the top and bottom panels representing  $1/4$  cycle (roughly a week) earlier and later, respectively. The top panel in this figure corresponds to the middle panel of Fig. 3 in AW1. In the top three panels of the left column of Fig. 2, a cold anomaly can be traced as it propagates downward through the lower stratosphere over the equator, above a layer of midtropospheric warm anomalies. This feature is the signature of a downward-propagating equatorial Kelvin wave. Upon reaching the tropical tropopause transition layer (TTL) in the third

panel, this feature widens and in the fourth panel it splits and is incorporated into the flanking Rossby wave signature to the west of the region of enhanced convection. In the fifth panel the centers of the cold anomaly lie atop the Rossby wave anticyclones, with even stronger warm anomalies below them, centered near the  $250\text{-hPa}$  level, extending out to  $\sim 50^\circ\text{N/S}$ . In all panels, the  $T$  and  $Z$  anomalies appear to be hydrostatically consistent.

The right panels of Fig. 2 describe the evolution of the vertical velocity field over the same location. The layer of ascent appears first at low levels (Fig. 2a), deepens, and becomes elevated until, half an MJO cycle later, it is replaced by low-level subsidence. The plume of ascent is initially confined to within  $10^\circ$  of the equator, but as it deepens and becomes elevated it widens out to  $15^\circ$ – $20^\circ\text{N/S}$  and it eventually splits. Secondary maxima in the amplitude of  $\omega$  are observed in the Rossby wave corridors [ $\sim 30^\circ$ – $35^\circ\text{N/S}$ ]. In these belts, maximum ascent occurs in Figs. 2b and 2c, after the passage of the coldest  $T$  perturbations in the flanking Rossby waves.

Figure 3 shows a partial zonal average of the mean structure of  $u$ ,  $v$ ,  $\omega$ , and  $T$ ,  $20^\circ$ – $60^\circ$  to the east and  $20^\circ$ – $60^\circ$  to the west of the longitude where  $\Delta\chi$  is a maximum.

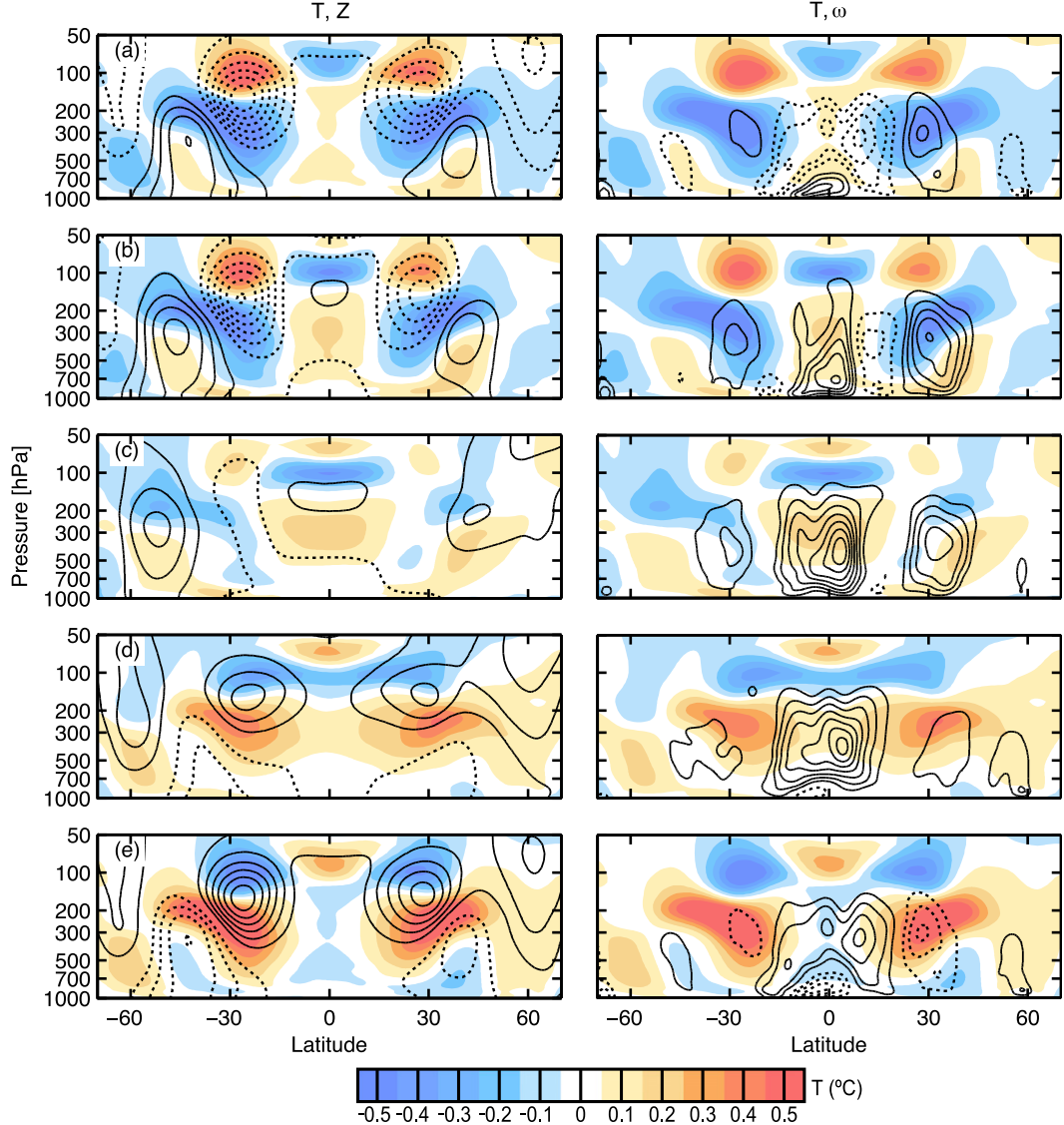


FIG. 2. Latitude–height cross section of (left)  $Z$  (contours) and  $T$  (shading) and (right)  $\omega$  (contours) and  $T$  (shading), averaged over the sector of longitude corresponding to the Maritime Continent ( $120^{\circ}$ – $150^{\circ}$ E) regressed on linear combinations of PC1 and PC2 of  $\Delta\chi$ : (a)  $-PC_2$ , (b)  $(PC_1 - PC_2)^{1/2}$ , (c)  $PC_1$ , (d)  $(PC_1 + PC_2)^{1/2}$ , and (e)  $PC_2$ . Contour interval 2 m for  $Z$  and  $1 \text{ hPa day}^{-1}$  for  $\omega$ . Ascent is depicted by solid contours and descent is depicted by dotted contours. The zero contour is omitted.

These cross sections are “warm pool composites” generated by averaging one-point regression maps at 1/64-cycle intervals over the half MJO cycle depicted in Fig. 2, zonally shifting each section in longitude so that the maximum in  $\Delta\chi$  lies over the reference longitude ( $0^{\circ}$ ). The cross sections are analogous to those in Fig. 2 but show the zonal mass flux ( $\rho u$ ) as contours and the meridional mass circulation ( $\rho v, \rho w$ ) as vectors. To the east of the  $\Delta\chi$  maximum (right panel) the structure is in many respects analogous to Fig. 2b. The broad, equatorially centered  $\rho u$  anomalies centered around 700 and

150 hPa are associated with the baroclinic modal structure described in AW1. In the lower troposphere the westerlies to the west of the heat source (i.e., the  $\Delta\chi$  maximum) shown in the left panel of Fig. 3 are stronger and more narrowly focused on the equator than the easterlies to the east of it. Consistent with the thermal wind equation, the corresponding temperature anomalies, warm to the east of the heat source and cold to the west, are centered in the layer of strongest vertical wind shear near the midtropospheric node in  $u$ . The vertical velocities are upward in the equatorial belt in both

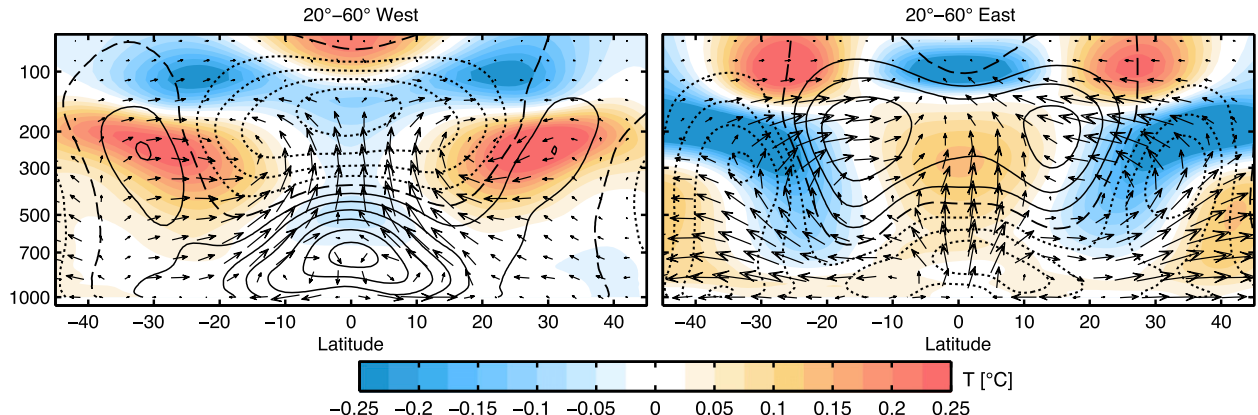


FIG. 3. Warm pool composite latitude–height cross sections of temperature (shading), zonal mass flux ( $\rho u$ , contours), and meridional mass circulation ( $\rho v, \rho w$ ) represented as vectors, partially zonally averaged from 20° to 60° to the (left) west and (right) east of the longitude at which  $\Delta\chi$  is a maximum. Warm pool composites are averages of a sequence of one-point regression maps within the sector ranging from 60°E to 180°. Each regression map is shifted zonally so that the  $\Delta\chi$  maximum lies on the reference longitude. Contour interval is  $0.1 \text{ kg m}^{-2} \text{ s}^{-1}$ . The  $\rho w$  component has been multiplied by 250 to make it consistent with the aspect ratio of the plot. The largest meridional flux vector is  $-0.1 \text{ kg m}^{-2} \text{ s}^{-1}$  and the largest vertical flux vector  $\sim 4 \times 10^{-4} \text{ kg m}^{-2} \text{ s}^{-1}$ . The zero value of  $u$  is depicted as a dashed contour.

sections, but the centroid of the ascent is more elevated to the west of the heat source than to the east of it. This distinction is consistent with the bottom-up development of the region of ascent in the right-hand panels of Fig. 2. Equatorially symmetric, lower-tropospheric meridional flows are clearly evident in both sections: equatorial outflow to the east of the heat source and inflow to the west of it. The center of mass is higher for the inflow than for the outflow. The near-surface confluent flow to the east contributes to the near-equatorial ascent while the diffluent flow to the west opposes it.

The top panel of Fig. 4 shows a warm pool composite longitude–height cross sections of  $T, \rho \times \text{Div}$  (shading), together with the overturning ( $\rho u, \rho w$ ) mass circulation, as represented by an average over the belt extending from 10°S to 10°N, indicated by vectors. The composite is constructed in the same manner as Fig. 3 and snapshots that constitute this warm pool composite can be found in the appendix (Fig. A1). Anomalies in  $T$  peak at 250 hPa  $\sim 20^\circ$  to the east of the reference longitude ( $0^\circ$ , maximum  $\Delta\chi$ ). East of this region where the  $T$  anomaly is a maximum, the  $T$  anomalies exhibit a pronounced eastward tilt with height above 250 hPa and a westward tilt with height below that level, giving rise to a “boomerang” shape (Wheeler et al. 2000). Regions of mass convergence lie beneath the positive  $T$  anomalies within a given region and exhibit a similar westward tilt with height. Above the region of maximum  $T$  anomalies in the 250-hPa layer is a region near 100 hPa where negative  $T$  anomalies appear in phase with divergence anomalies, consistent with the structure of free Kelvin waves (see appendix for further discussion). Similar, but less distinct, features are seen to the west of the reference longitude.

The zonal mass circulation in this composite, which is reminiscent of Fig. 16 of Madden and Julian (1972), exhibits even zonal symmetry with respect to the reference longitude, as defined by the  $\Delta\chi$  maximum.

The other panels in Fig. 4 depict the mass divergence field broken down into its zonal wind component ( $\rho \partial u / \partial x$ ; Fig. 4b) and meridional wind component ( $\rho \partial v / \partial y$ ; Fig. 4c). The contribution from  $\partial u / \partial x$  is dominant near the reference longitude but elsewhere both terms are important. The  $\partial u / \partial x$  field exhibits a single node near the 400-hPa level, with convergence throughout the lower troposphere centered at 800 hPa. In contrast,  $\partial v / \partial y$  exhibits a more complex vertical structure with two nodes: one at the top of the boundary layer near 850 hPa and a second in the midtroposphere. The largest amplitudes in  $\partial v / \partial y$  are located within the boundary layer ( $\sim 975$ ) hPa and near the 600- and 150-hPa levels. It is notable that neither  $\partial u / \partial x$  nor  $\partial v / \partial y$  exhibits a vertical tilt but they are juxtaposed zonally in such a way that the total divergence field exhibits a substantial vertical tilt.

The temperature and vertical velocity fields in the flanking Rossby waves are shown in the top panel of Fig. 5 in the form of longitude–height cross sections analogous to those Fig. 4, but for the 30°–35°N and 30°–35°S latitude belts, where secondary peaks in the amplitude of the MJO-related  $\omega$  perturbations in Fig. 1 and the right column of Fig. 2 are observed. The longitudinal sectors that are anomalously cold at the 250-hPa level and warm at the 100-hPa level correspond to the lows in the 150-hPa height field in the flanking Rossby waves and vice versa. Deep ascent prevails directly below the equatorward 150-hPa flow to the west of the lows in 150-hPa Z. Barlow et al. (2005) and Hoell et al. (2012)

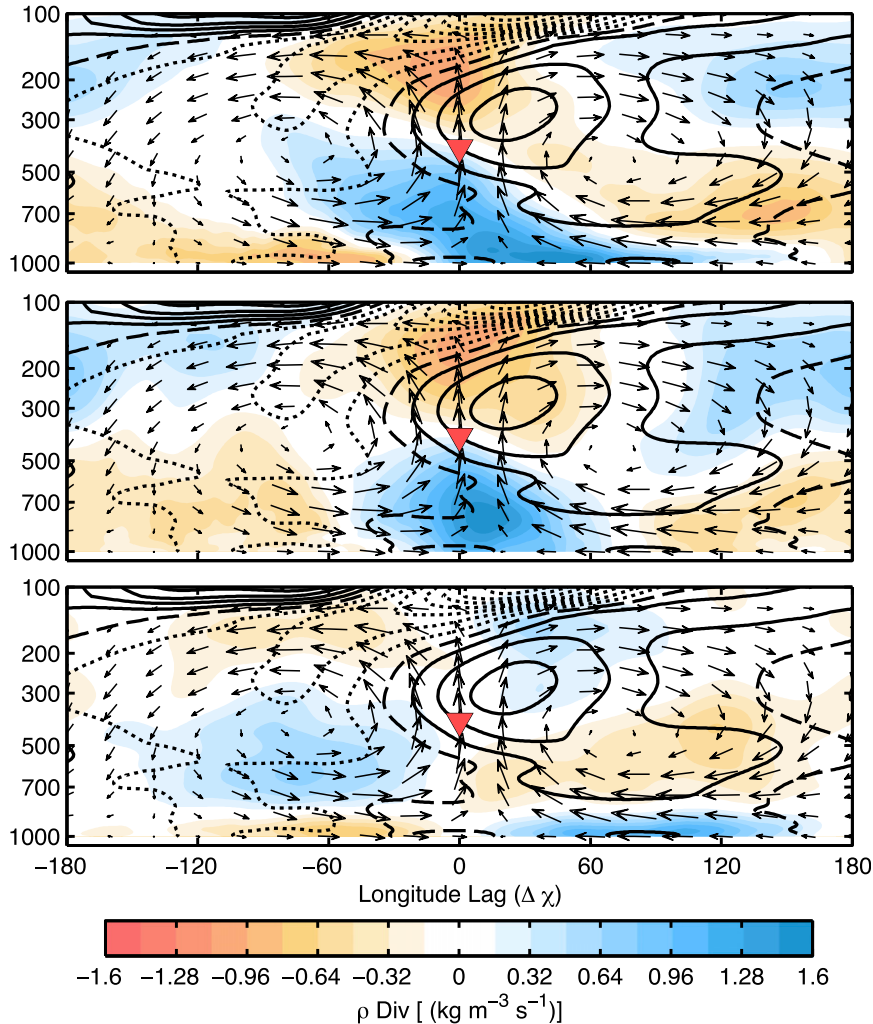


FIG. 4. Warm pool composite equatorial ( $10^{\circ}\text{S}$ – $10^{\circ}\text{N}$ ) vertical cross sections of temperature (contours) and (top) mass divergence  $\rho \times \text{Div}$ , (middle)  $\rho \partial T / \partial \chi$ , and (bottom)  $\rho \partial T / \partial \chi$ . Vectors depict zonal equatorial mass circulation ( $\rho u$ ,  $\rho w$ ). Contour interval is  $0.05^{\circ}\text{C}$ . The red triangle indicates the maximum in  $\Delta\chi$ . The  $\rho w$  component has been multiplied by a factor of 250. The largest zonal flux vector is  $\sim 0.6 \text{ kg m}^{-2} \text{ s}^{-1}$ , and the largest vertical flux vector is  $\sim 7 \times 10^{-4} \text{ kg m}^{-2} \text{ s}^{-1}$ . The zero value of  $T$  is depicted as a dashed contour. The sign of  $\text{Div}$  has been flipped for presentation.

found a near balance between the temperature tendencies induced by vertical motion in the flanking Rossby waves over southern Asia and the horizontal temperature advection ( $\mathbf{V} \cdot \nabla T$ ). A similar balance is evident in the bottom panels of Fig. 5, in which the vertical velocity anomaly term is represented by  $S_p \omega^*$ , where  $S_p = 5 \times 10^{-4} \text{ K Pa}^{-1}$  [see section 6.2.1 of Holton (2004)] is the dry static stability parameter in pressure coordinates and the horizontal advection term is approximated by the component associated with the zonally averaged zonal wind; that is,  $[\bar{u}] \partial T^* / \partial x$ , where  $T^*$  is the temperature anomaly associated with the flanking Rossby waves. This near balance suggests that the

MJO-related vertical motions in the Rossby wave corridors are, to first order, characterized by zonal flow along the undulating isentropic surfaces.

#### 4. Modal analysis of the MJO-related temperature and vertical velocity fields

In this section, we decompose the three-dimensional MJO-related temperature ( $T$ ) and vertical velocity ( $\omega$ ) fields into modal structures with orthogonal vertical profiles as in section 4 of AW1, but using EOF analysis rather than MCA. As in AW1, the analysis is carried out using all grid points within the equatorial band  $10^{\circ}\text{S}$ – $10^{\circ}\text{N}$ .

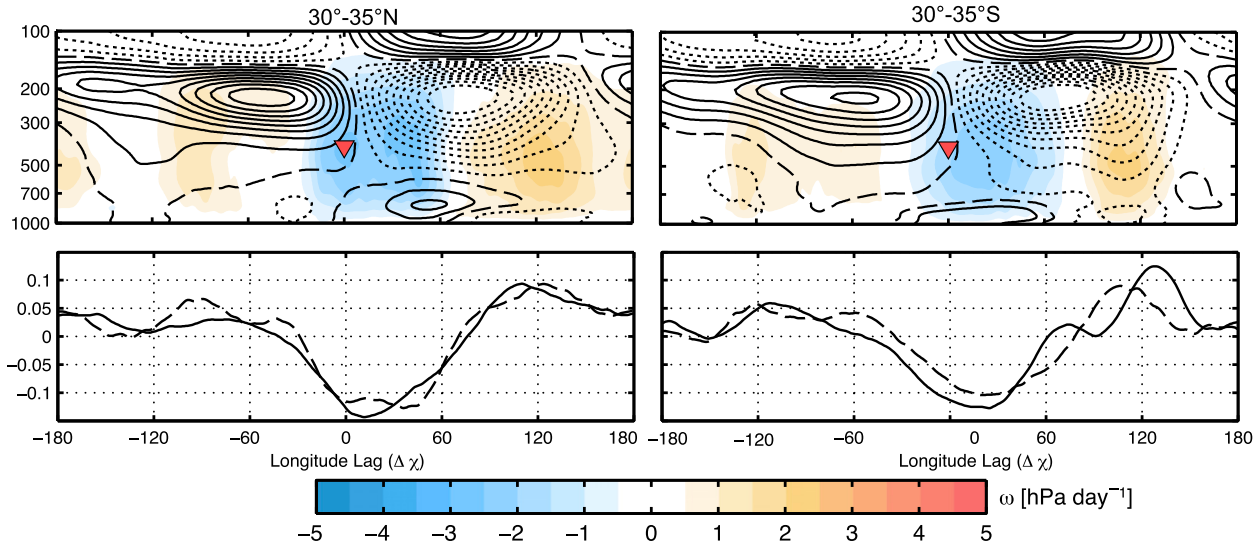


FIG. 5. (top) Warm pool composite latitude–height cross sections of temperature (contoured) with vertical velocity (shaded) for the latitude bands (left) 30°–35°N and (right) 30°–35°S. Contour interval is 0.05°C. The zero value of  $T$  is depicted as a dashed line. The red triangle indicates the maximum in  $\Delta\chi$ . (bottom) Plots of  $[\bar{u}]\partial T^*/\partial x$  (solid) and  $S_p\omega^*$  (dashed) averaged over the 200–500-hPa layer ( $^{\circ}\text{C day}^{-1}$ ).

We have verified that the results that we will focus on here are nearly perfectly reproducible in domains extending out to 30°N/S.

The leading mode of the  $T$  expansion is shown in the left panel of Fig. 6. EOF1, referred to here as  $T_1$ , accounts for 63% of the variance of the stack of  $T$  regression patterns. It is characterized by anomalies of opposing polarity in layers centered around the 250- and 100-hPa levels. The pattern for  $T_1$  is closely associated with the geopotential height pattern of the leading modal structure in AW1, referred to here as  $(u_1, Z_1)$ . The quantity  $T_1$  is related to  $(u_1, Z_1)$  through the hydrostatic and thermal wind equations and exhibits a structure similar to the vertical profiles discussed by Holloway and Neelin (2007). The second mode,  $T_2$  (not shown), accounts for more than half of the remaining variance but it mainly accounts for temperature variations in the TTL and lower stratosphere and will not be discussed further.

The leading mode of the vertical motion field,  $\omega_1$ , which accounts for 72% of the variance, is indicated by the solid line in the right panel of Fig. 6. It is of the same polarity at all levels and mirrors the vertical profile of rms amplitude of  $\omega$  (not shown). The second mode,  $\omega_2$ , which accounts for another 18% of the variance, plays the role of a shape parameter. It is characterized by perturbations of opposing polarity above and below 600 hPa. The EOFs of vertical velocity have the same shape as the EOFs of latent heating obtained by Zhang and Hagos (2009). The vertical profiles of  $\omega_1$  and  $\omega_2$  are also analogous to linear combinations of the “deep convective” and “elevated stratiform” categories used by Houze (1982, 1989), Schumacher et al.

(2004), Haertel et al. (2008), and others to characterize latent heating profiles in convective systems.

The top panel of Fig. 7 shows a warm pool composite of the spatial structure of  $T_1$ , represented by contours and scaled to the 250-hPa level, superposed on OLR (shading). The composite is constructed in the same manner as Figs. 3 and 4. The horizontal pattern in  $T_1$  is nearly identical to the modal structure  $(u_1, Z_1)$  in Fig. 6 of AW1. It also resembles the 100-hPa temperature pattern shown in Fig. 3 of Virts and Wallace (2014). The most striking features in this pattern are associated with the flanking Rossby waves along 28°N/S, but features reminiscent of the equatorial Kelvin wave can be seen east and west of the reference longitude. As in the  $u$  and  $Z$  patterns in the modal structure shown in Fig. 6 of AW1, the regression patterns for  $T_1$  are bowed forward (eastward) along the equator. Thus, the structure in  $T_1$  can be interpreted as the thermal signature of the planetary wave structure associated with the MJO. It can also be interpreted as the temperature signature of a convectively coupled mode because a virtually identical temperature profile emerges as the leading MCA mode when  $T$  is paired with  $\omega$ , accounting for 72% of the squared covariance between  $T$  and  $\omega$  in the stack of regression maps (not shown).

The middle and bottom panels of Fig. 7 show the horizontal distributions of  $\omega_1$  (middle panel) and  $\omega_2$  (bottom panel), as obtained through the warm pool compositing described above. The horizontal maps of  $\omega_1$  and  $\omega_2$  are scaled to their corresponding PC values at the 300-hPa level (see Fig. 6). Negative values of  $\omega_1$  and  $\omega_2$

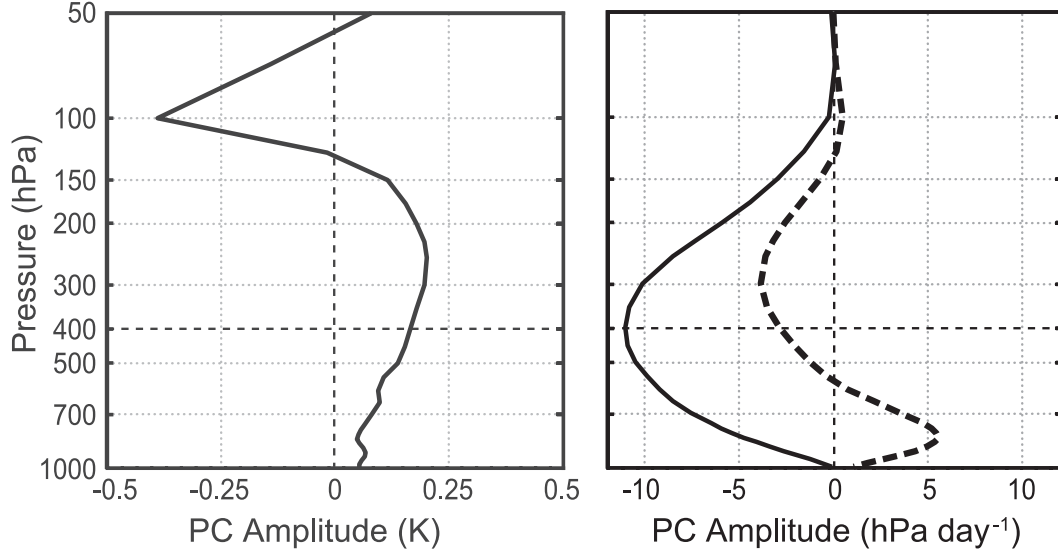


FIG. 6. Leading principal components (PCs) of (left)  $T$  and (right)  $\omega$  derived from EOF analysis of the vertical profiles of  $T$  and  $\omega$  regressed on PC1 and PC2 of  $\Delta\chi$  as explained in the text. The analysis is based on grid points in the  $10^{\circ}\text{S}$ – $10^{\circ}\text{N}$  latitude belt. The solid line denotes the first mode and the dashed line denotes the second mode. The PCs are scaled in proportion to their eigenvalues and expressed in units of  $^{\circ}\text{C}$  for  $T$  and  $\text{hPa day}^{-1}$  for  $\omega$ . By convention, negative values of  $\omega_1$  and  $\omega_2$  are indicative of ascent. The dimensional values are representative of amplitudes of  $1\sigma$  of the respective PC time series.

indicate ascent at this level. The horizontal wind and  $Z$  fields vertically averaged over the 500–1000-hPa layer are also displayed in these two panels. As expected, the patterns for leading mode  $\omega_1$  resemble the corresponding OLR patterns (top panel) but are simpler and easier to interpret. Consistent with the widening of the plume of enhanced ascent with time in the right column of Fig. 2, the colored patches denoting anomalous ascent–descent are bowed forward (eastward) along the equator along their eastern edge and they widen and split toward their western edge. These off-equatorial  $\omega_1$  anomalies are most clearly defined  $30^{\circ}$ – $60^{\circ}$  to the west of the reference longitude where the equatorial westerlies exhibit sharp edges; that is, bands of strong meridional shear ( $\partial u/\partial y$ ) centered over  $10^{\circ}$ – $20^{\circ}\text{N/S}$ . In comparison, anomalies in  $\omega_2$  (bottom panel) are weaker and more narrowly focused on the equator, exhibiting an out-of-phase relationship with anomalies in lower-tropospheric  $u$ . Readers interested in the evolution of  $T_1$ ,  $\omega_1$ , and  $\omega_2$  in the MJO cycle can refer to the five-panel sequences in the appendix (Fig. A2).

Along the equator the patterns for  $\omega_2$  (Figs. 7 and A2) tend to be zonally displaced relative to the  $\omega_1$  centers, with shallow convection to the east of the regions of enhanced convection, and elevated stratiform convection to the west of them. Since the MJO-related features tend to be eastward propagating, the structures of  $\omega_1$  and  $\omega_2$  (Figs. 7 and A2) are indicative a systematic bottom-up

evolution of the vertical motion profile at a fixed point, consistent with the sequence shown in Fig. 2 (and with Fig. A3 in the appendix). To define the domain in which this characteristic behavior is observed, we performed a pointwise analysis of the degree to which  $\omega_1$  and  $\omega_2$  tend to appear in quadrature in the MJO cycle with  $\omega_1$  leading  $\omega_2$ , as defined by the relationship

$$W_{\perp}(\omega_1, \omega_2) = \omega_{11}\omega_{22} - \omega_{12}\omega_{21}. \quad (2)$$

Here  $\omega_{11}$  refers to the regression map for  $\omega_1$  regressed on PC1 of  $\Delta\chi$ , etc. The results are shown in the top panel of Fig. 8. In this plot positive values (green shading) indicate the regions in which this bottom-up evolution prevails. The strongest positive values of  $W_{\perp}$  are observed over the Indo-Pacific warm pool but weaker positive values prevail throughout much of the region equatorward of  $10^{\circ}\text{N/S}$ . Poleward of  $10^{\circ}\text{N/S}$ , there is no tendency for  $\omega_1$  to lead  $\omega_2$ .

The features in  $\omega_2$  along the equator appear to occur in close association with features in the low-level zonal flow, as shown in Fig. 7. The bottom panel of Fig. 8 shows the dot product of lower-tropospheric  $u$  and  $\omega_2$ , indicative of the degree to which these fields tend to appear in phase in the MJO cycle, as defined by the relationship

$$W_{\parallel}(u, \omega_2) = u_1\omega_{21} + u_2\omega_{22}. \quad (3)$$

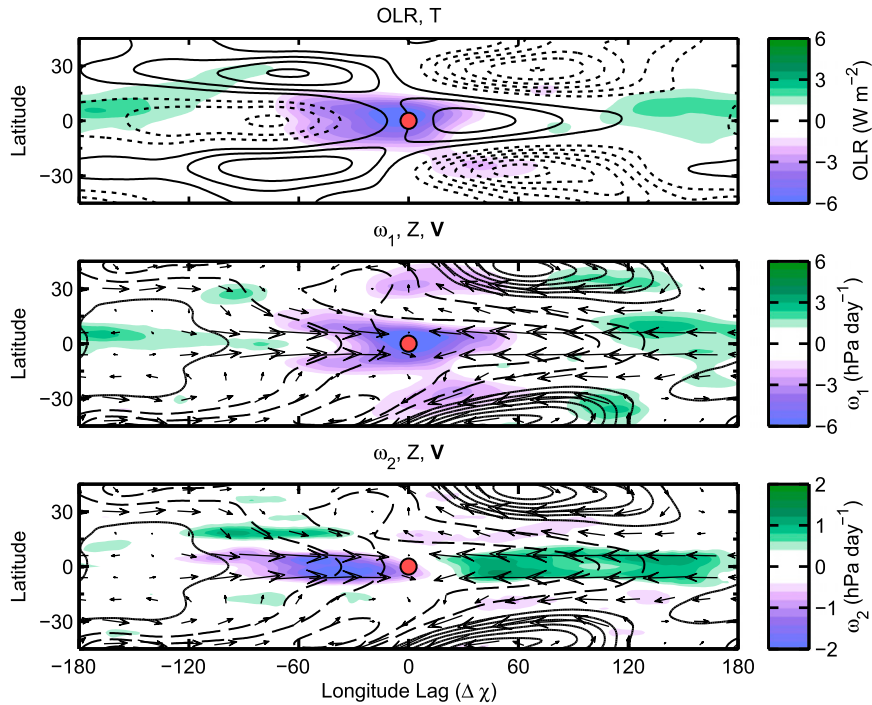


FIG. 7. (top) Warm pool composite of  $T_1$  (contours) superimposed upon OLR (shading). Contour interval is  $0.05^\circ\text{C}$ .  $T_1$  scaled to the 250-hPa level. (middle),(bottom) Warm pool composite of 500–1000-hPa layer-averaged winds (vectors),  $Z$  (contours),  $\omega_1$  (shading), and  $\omega_2$  (shading). Contour interval is 1 m. The  $\omega_1$  and  $\omega_2$  are scaled to the 300-hPa level. The largest wind vector is  $\sim 0.75 \text{ m s}^{-1}$ . The red circle indicates the maximum in  $\Delta\chi$ .

Negative values (red shading) are indicative of an in-phase relationship between westerly wind anomalies and negative  $\omega_2$  anomalies. That the patterns associated with  $W_{\parallel}$  are nearly identical to those associated with  $W_{\perp}$  indicates that throughout the equatorial belt a systematic bottom-up evolution in anomalous ascent is inextricably linked to the evolution of lower-tropospheric zonal wind in the MJO cycle. In the zonally averaged profiles shown in the right panels of Fig. 8, it is clear that these relationships are strongest near the equator and decay to zero at  $\sim 10^\circ$  from the equator. In the next section, we will explore the mechanisms that lead to the systematic evolution in the  $\omega$  field in the equatorial belt and the dynamical processes that are responsible for the characteristic “swallowtail pattern” in  $\omega_1$ .

## 5. Dynamical controls on the vertical velocity field

Because friction influences the observed structure of the divergence field (Wang 1988; Wang and Li 1994; Maloney and Hartmann 1998; Hsu and Li 2012), we will consider separately the part of the divergence occurring within the boundary layer (BL; the 850–1000-hPa layer) and the part occurring in the lower free troposphere

(FT; the 500–850-hPa layer). The distributions of Div, wind, and  $Z$  averaged over these layers are shown in Fig. 9. In the FT, Div is concentrated within the equatorial belt. To the east of the strongest convergence, the winds are easterly, while a narrower belt of equatorial westerlies prevails to the west of it. The near-equatorial wind field exhibits a significant meridional component, with poleward motion to the east of the reference longitude and equatorward motion to the west of it—a feature that is not apparent when the winds are averaged over the 500–1000-hPa layer as in Fig. 7.

In the BL, the effects of friction cause the divergence anomalies to assume a different shape, with maximum BL convergence shifted  $\sim 35^\circ$  of longitude to the east of the strongest FT convergence. The region of BL convergence to the east of the main region of convection has been noted in previous studies of Lau et al. (1988), Hendon and Salby (1994), Maloney and Hartmann (1998), and Hsu and Li (2012), among others, and has been attributed to frictionally induced meridional confluence in the equatorial Kelvin wave. In the BL the easterlies to the east of the reference longitude exhibit a significant equatorward component, which is consistent with this interpretation, but we have not established that it is entirely a Kelvin wave signature.

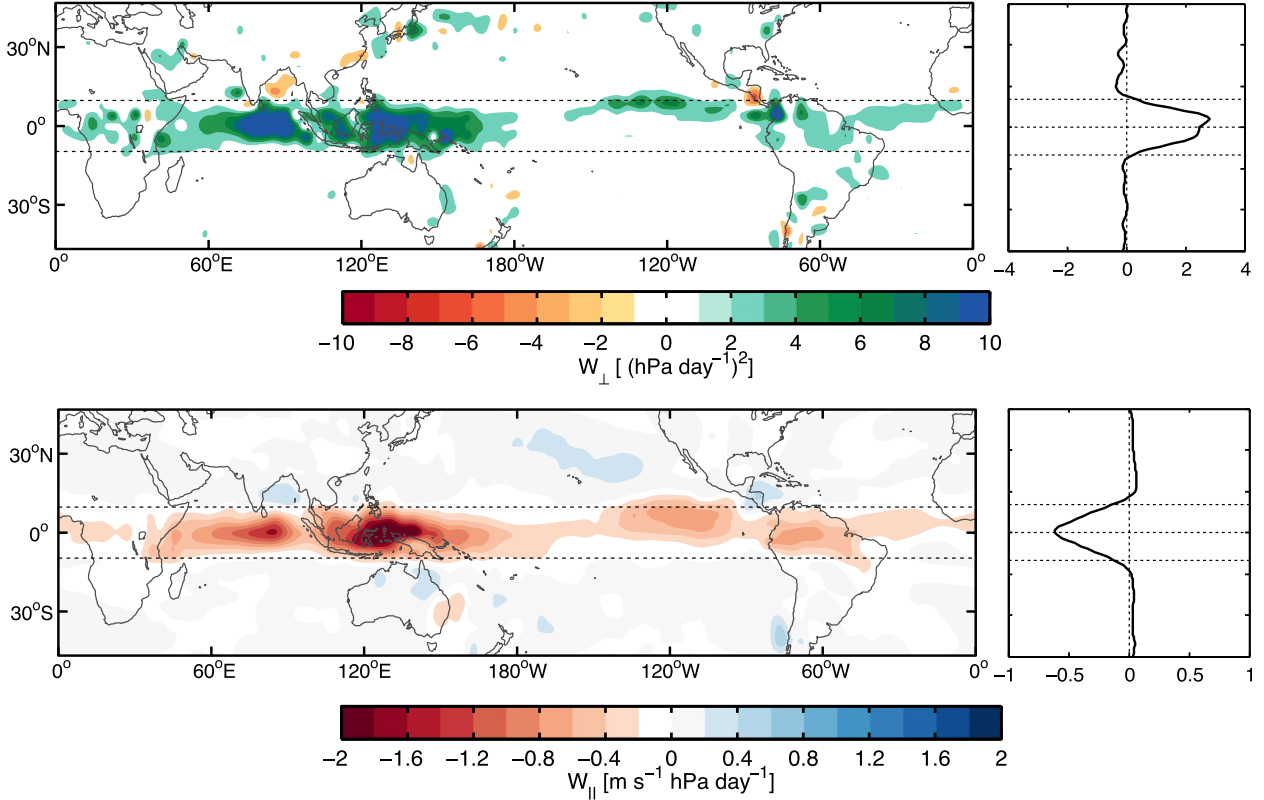


FIG. 8. (top) (left) Spatial distribution of the 1/4-cycle-lagged covariance  $W_{\perp}$  between  $\omega_1$  and  $\omega_2$  as defined by Eq. (2) and (right) zonally averaged profile of  $W_{\perp}$ . (bottom) (left) Spatial distribution of the cross covariance  $W_{\parallel}$  between lower-tropospheric  $u$  and  $\omega_2$  as defined by Eq. (3) and (right) zonally averaged profile of  $W_{\parallel}$ . The 10°N and 10°S latitudes are marked by dotted lines.

In both the FT and the BL, the easterlies to the east of the reference longitude extend poleward beyond  $\sim 30^{\circ}\text{N/S}$ . They are bracketed by anticyclones along  $\sim 45^{\circ}\text{N/S}$ , as noted by Adams et al. (2014). To the west, in the region of maximum large-scale convergence lies a patch of equatorial BL divergence flanked by off-equatorial convergence ( $\sim 18^{\circ}\text{N/S}$ ). In this region, the meridional flow in the equatorial belt is strongly diffluent. The off-equatorial convergence lines to the west of the reference longitude, in combination with the equatorial convergence to the east of it, conspire to create the characteristic swallowtail pattern in  $\omega_1$  (Fig. 7).

Figure 10 shows the FT and BL components of the horizontal divergence,  $\partial u / \partial x$  (left panels) and  $\partial v / \partial y$  (right panels). The FT convergence is dominated by  $\partial u / \partial x$ . The secondary contribution from  $\partial v / \partial y$  acts to shift the region of maximum convergence westward. Poleward of  $15^{\circ}\text{N/S}$   $\partial u / \partial x$  and  $\partial v / \partial y$  tend to cancel one another so that the flow is quasi nondivergent. In the BL,  $\partial u / \partial x$  is slightly weaker than in the FT and exhibits a hint of a swallowtail pattern, which may be a reflection of the fact that the westerly anomalies to the west of the reference longitude are more narrowly confined to the

equatorial belt than the easterly wind anomalies to the east of it. But it is clear from Fig. 10 that the BL  $\partial v / \partial y$  is mainly responsible for the swallowtail pattern in BL Div in Fig. 9. The equatorial convergence to the east of the reference longitude and the divergence to the west of it are attributable to frictional convergence in the lower-tropospheric easterlies to the east of the reference longitude and westerlies to the west of it. The convergence lines along  $18^{\circ}\text{N/S}$  to the west of the reference longitude mark the boundary between the diffluent equatorial westerlies and the confluent westerly flow in the Rossby wave in the FT, which is also clearly discernible in Fig. 3.

Wang and Rui (1990), Wang and Li (1993), and Moskowitz and Bretherton (2000) have shown that the MJO-related BL convergence is well represented by the Laplacian of the low-level geopotential field ( $\phi = gZ$ ) in equatorial planetary waves, augmented by the term representing the divergence of the Coriolis parameter in the momentum equations [i.e.,  $\nabla \cdot (f\mathbf{k} \times \mathbf{u})$ ], as represented in the expression derived in Wang and Li (1994):

$$\text{Div}_{\text{BL}} \approx \frac{-\epsilon}{\epsilon^2 + \beta^2 y^2} \left( \nabla^2 \phi + \beta u + \frac{\beta^2 y v}{\epsilon} \right), \quad (4)$$

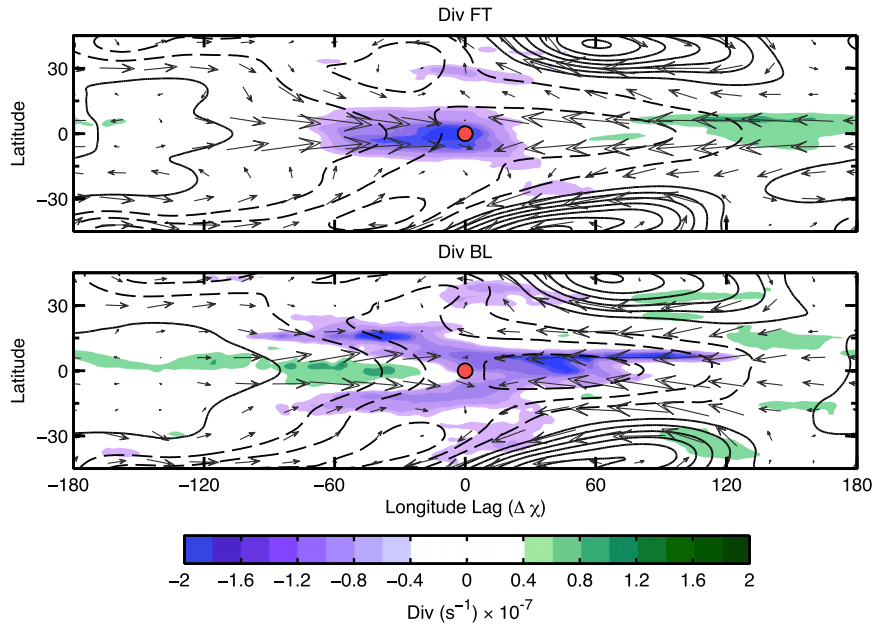


FIG. 9. (top) Warm pool composite of lower-FT (500–850 hPa) layer-averaged divergence (shading), wind (vectors), and geopotential height (contours) anomalies. (bottom) As in (top), but averaged over the BL (850–1000 hPa). Contour interval is 1 m. The largest wind vector is  $\sim 0.75 \text{ m s}^{-1}$ . The red circle indicates the maximum in  $\Delta\chi$ .

where  $\epsilon = 2.6 \text{ day}^{-1}$  is the Raleigh friction coefficient, chosen to be consistent with results of studies by Deser (1993), Li and Wang (1994), and Stevens et al. (2002), and  $\beta = 2.28 \times 10^{-11} \text{ m}^{-1} \text{s}^{-1}$  is the beta parameter. The top panel of Fig. 11 shows the Laplacian of the BL geopotential field, scaled to units of per second. It is dominated by a broad negative region to the east of the reference longitude and a narrower, positive region flanked by negative anomalies over the outer tropics to the west, similar to the BL divergence field in the bottom panel of Fig. 9. It differs from the observed BL divergence field in the sense that the amplitudes are larger and the negative anomalies east of the reference longitude cover a much larger area, and the anomalies to the west of the reference longitude are broader in meridional extent. When the beta effect is taken into account, the calculated  $\text{Div}_{\text{BL}}$  more closely resembles the observed  $\text{Div}_{\text{BL}}$  but the amplitudes are still larger. Hence, we can conclude that the structure of BL divergence is, to first order, driven by planetary-scale wave motions in the presence of frictional drag.

If motions in the BL and lower FT are responsible for the observed structure in  $\omega_1$  and  $\omega_2$ , then it should be possible to represent the patterns of  $\omega_1$  and  $\omega_2$  in terms of linear combinations of  $\text{Div}_{\text{FT}}$  and  $\text{Div}_{\text{BL}}$ . The deep convective profile,  $\omega_1$ , is of the same sign at all levels, peaking at 400 hPa. It follows from the conservation of mass

that convergence should prevail throughout the entire lower troposphere in regions where  $\omega_1$  dominates. In regions where  $\omega_2$  is dominant, divergence should be of opposing sign above and within the BL. Hence, we anticipate that

$$\omega_1 \propto \text{Div}_{\text{FT}} + \text{Div}_{\text{BL}} \quad \text{and} \quad (5a)$$

$$\omega_2 \propto \text{Div}_{\text{FT}} - \text{Div}_{\text{BL}}. \quad (5b)$$

The left column of Fig. 12 confirms that the patterns for the left and right hand sides of Eqs. (5a) and (5b) are indeed very similar. It is notable that  $\omega_2$  is strongly equatorially trapped because it is only in that region that  $\text{Div}_{\text{FT}}$  and  $\text{Div}_{\text{BL}}$  are of opposing sign. This explains why a systematic evolution in  $\omega$  from shallow convection, to deep and elevated stratiform during the MJO cycle, occurs only within the equatorial belt. Moreover, because  $\partial u / \partial x$  is the term that tends to be of the same polarity above and below the top of the BL (Fig. 4), the  $\text{Div}_{\text{FT}} + \text{Div}_{\text{BL}}$  term is dominated by zonal wind component of horizontal divergence ( $\partial u / \partial x$ ; top right panel of Fig. 12), while the regions of divergence of opposing sign above and below the BL, which are associated with  $\omega_2$ , are dominated by the meridional wind component ( $\partial v / \partial y$ ; bottom right panel of Fig. 12).

The steady-state response to equatorial heating, as described by Matsuno (1966) and Gill (1980) and herein

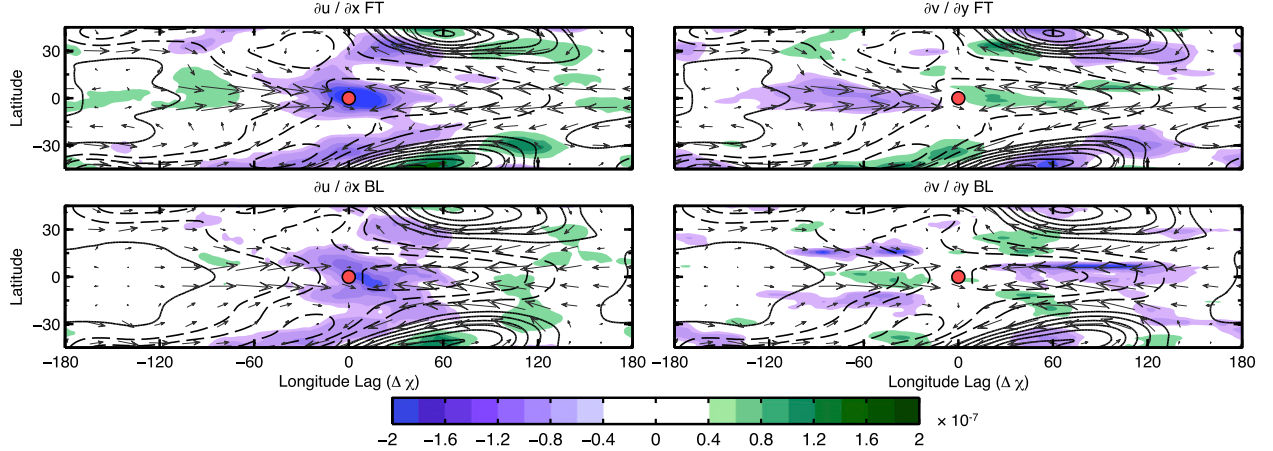


FIG. 10. As in Fig. 9, except the shading depicts (top) (left) FT  $\partial u / \partial x$  and (right)  $\partial v / \partial y$  and (bottom) (left) BL  $\partial u / \partial x$  and (right)  $\partial v / \partial y$ . Contour interval is 1 m. The largest wind vector is  $\sim 0.75 \text{ m s}^{-1}$ . The red circle indicates the maximum in  $\Delta\chi$ .

referred to as the “Matsuno–Gill model,” is shown in Fig. 13. The planetary wave response to an isolated equatorial heat source is obtained from the following set of differential equations:

$$\frac{\partial u}{\partial t} = \beta y v - \frac{\partial \phi}{\partial x} - \epsilon u, \quad (6a)$$

$$\frac{\partial v}{\partial t} = -\beta y u - \frac{\partial \phi}{\partial y} - \epsilon v, \quad (6b)$$

$$\frac{\partial \phi}{\partial t} = -gH \left( \frac{\partial u}{\partial x} + \frac{\partial v}{\partial y} \right) + gQ(x, y) - \epsilon\phi, \quad \text{and} \quad (6c)$$

$$Q(x, y) = Q_0 \exp \left[ -\frac{(x - x_0)^2}{\sigma_x^2} - \frac{(y - y_0)^2}{\sigma_y^2} \right], \quad (6d)$$

where  $Q_0 = 100 \text{ m day}^{-1}$ ,  $\epsilon = 0.1 \text{ day}^{-1}$ ,  $H = 200 \text{ m}$ ,  $\sigma_x = 5.2 \times 10^6 \text{ m}$ ,  $\sigma_y = R_e (10 \times 10^5 \text{ m})$ ,  $x_0 = y_0 = 0$ , and where  $R_e$  is the equatorial Rossby radius of deformation, values similar to those chosen by Gill (1980), Kraucunas and Hartmann (2007), and Bao and Hartmann (2014). It is

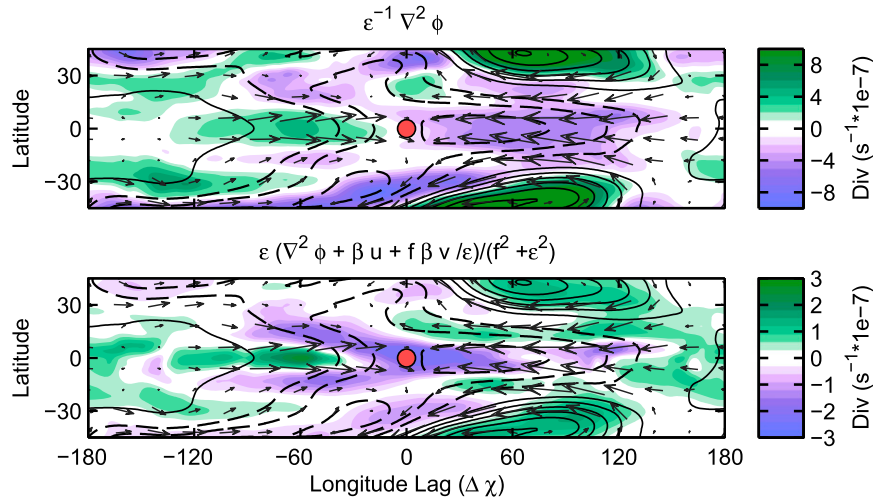


FIG. 11. Estimates of BL divergence based on Eq. (4). The shading depicts (top)  $\epsilon^{-1} \nabla^2 \phi$ , where  $\phi$  is the geopotential field at the 850–1000-hPa level, and (bottom)  $\text{Div}_{\text{BL}}$  calculated applying Eq. (4) to the observed BL (850–1000-hPa layer averaged)  $Z$ ,  $u$ , and  $v$  fields. Contour interval is 1 m. The largest wind vector is  $\sim 0.75 \text{ m s}^{-1}$ . The red circle indicates the maximum in  $\Delta\chi$ .

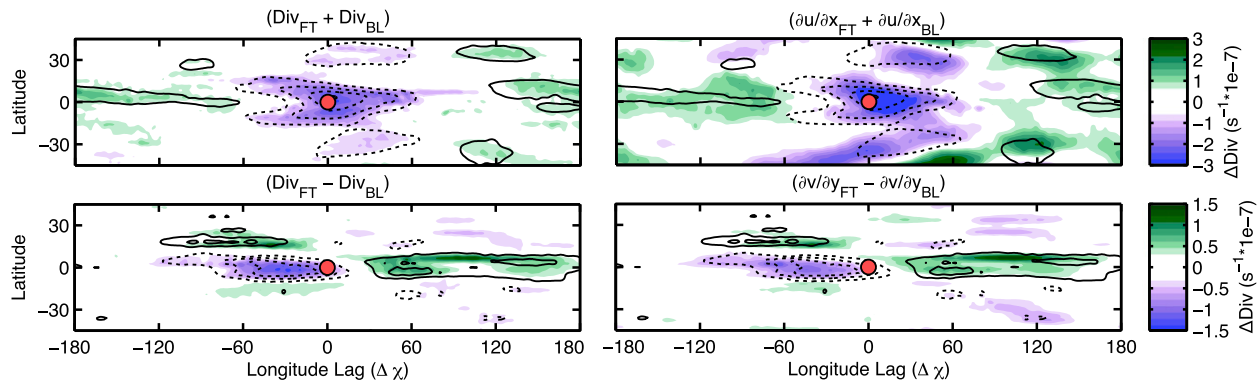


FIG. 12. (top) Warm pool composite of  $\omega_1$  scaled to the 300-hPa level (contours) and (left) the sum of FT and BL divergence and (right) the sum of FT and BL  $\partial u/\partial x$  (shading). Contour interval is  $1.5 \text{ hPa day}^{-1}$ . (bottom) Warm pool composite of  $\omega_2$  scaled to the 300-hPa level (contours) and (left) the difference between FT and BL divergence and (right) the difference between FT and BL  $\partial v/\partial y$  (shading). Contour interval is  $0.5 \text{ hPa day}^{-1}$ . The red circle indicates the maximum in  $\Delta\chi$ .

worth mentioning that even though the MJO exhibits a dipolar structure in heating throughout most of its life cycle, as documented in AW1 and in the appendix, we choose to present the solution for the response to an isolated heat source because it can be viewed as a simple “building block” from which the patterns in all phases of the MJO cycle can be constructed. The response to a dipole heat source, shown in the right column of Fig. 13, is virtually identical to a superposition of the response to two monopoles of opposing signs with the same spacing as the dipole, which was chosen to be  $90^\circ$  in the case of Fig. 13 so it closely corresponds to the spacing of the  $\omega_1$  anomalies at the time when PC2 of  $\Delta\chi$  is a maximum.

The  $\nabla^2\phi$  fields in the observations (Fig. 11) and the Matsuno–Gill model (Fig. 13b) exhibit qualitatively similar structures, with a swath of negative anomalies to the east of the heat source. To the west of the heat source it splits into two off-equatorial convergence lines flanking a region of positive anomalies. The observed and simulated patterns differ in the sense that the observed  $\nabla^2\phi$  field is meridionally more extensive and the anomalies to the east of the reference longitude are larger in amplitude than the anomalies to the west of it. The horizontal maps of  $\partial u/\partial x$  and  $\partial v/\partial y$  in the corresponding FT pattern (top panels of Fig. 10) also exhibit similar structures to their counterparts in the Matsuno–Gill solution (Figs. 13b and 13c). Thus, it can be said that the structure of vertical motion field within  $20^\circ$  of the equator resembles the steady-state response to an equatorial heat source.

## 6. Discussion

The analysis in AW1 and in the present paper is largely based on the following methodology:

- The  $u$ ,  $Z$ ,  $T$ ,  $\omega$ , and Div fields are regressed upon linear combinations of the leading PCs of the global daily  $\Delta\chi$  field.
- The evolving three-dimensional patterns these fields in the MJO cycle are characterized in terms of modal structures [i.e., separable functions of  $(x, y)$ , and  $p$ , as defined in Eq. (2) of AW1].
- Warm pool composites are used to represent the mean structure of the MJO during the half of its cycle when the convection is most active.

While many of the features that emerge in our analyses have been pointed out in previous studies, seeing them displayed in a simple, consistent format with minimal sampling variability lends new insight into the structure and dynamics of the MJO.

Findings reported in AW1 relate mainly to the upper-tropospheric structure as manifested in the  $u$  and  $Z$  fields. The observed MJO structure in the equatorial belt exhibits the signature of a Kelvin wave, in which the leading edge of an advancing patch of easterly winds coincides with the maximum in  $\Delta\chi$  and the centroid of the enhanced convection. The dominant features at subtropical latitudes ( $20^\circ$ – $40^\circ\text{N/S}$ ) are planetary-scale gyres centered on  $28^\circ\text{N/S}$ , just equatorward of the axes of the climatological-mean westerly jet streams. In recognition of the fact that these centers lie within the shear zones along the outer edges of the eastward-propagating MJO-related zonal wind anomalies, we have referred to them as the “flanking Rossby waves.” In AW1 we postulated that these features, which are not explained by the linear theory of planetary waves on an equatorial beta plane in an atmosphere at rest, owe their existence to the strong meridional and vertical shears in the zonal mean background flow.

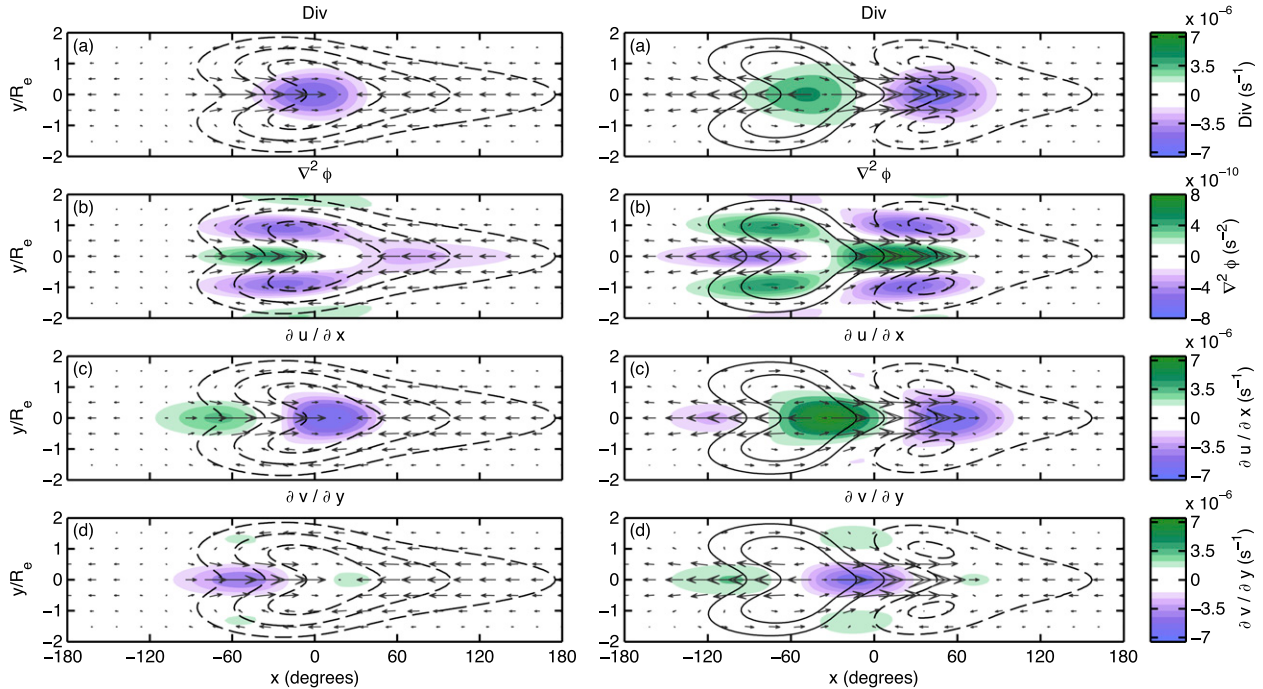


FIG. 13. Gill–Matsuno model solutions for (left) an isolated equatorial heat source located at  $0^\circ$  and (right) a dipole heat source–sink separated by  $90^\circ$ . See text for further details. The quantity  $Z$  is contoured and the shaded fields are labeled in each row: (a) divergence and (b) Laplacian of geopotential ( $\nabla^2 \phi$ ), (c)  $\partial u / \partial x$ , and (d)  $\partial v / \partial y$ . Contour interval is 10 m. The largest wind vector is around  $10 \text{ m s}^{-1}$ . The  $y$  axis is normalized by the equatorial Rossby radius of deformation  $R_e$ .

In the present study (AW2), the same flanking Rossby waves are observed in the leading modal structure in the temperature field  $T_1$ . They are also associated with a secondary maximum in the amplitude of the MJO-related  $\omega$  field at the latitude of the climatological-mean jet streams ( $30^\circ\text{--}35^\circ\text{N-S}$ , Fig. 1). The wave in the vertical velocity field in this latitude belt is associated with zonal flow along sloping isentropes (Fig. 5).

The main findings in AW2 relate to the equatorial lower troposphere. The analysis reveals the existence of shallow, frictionally driven mean meridional circulation cells embedded in the zonal overturning cells to the east and west of the regions of enhanced convection. Both the zonal overturning and the meridional overturning contribute to the divergence field—the former through the  $\partial u / \partial x$  term and the latter through the  $\partial v / \partial y$  term. Neither the  $\partial u / \partial x$  pattern nor the  $\partial v / \partial y$  pattern exhibits a significant westward tilt with height in the equatorial plane in its own right, but when the two components are juxtaposed to form the divergence field a significant westward tilt with height is observed.

The analysis clearly reveals the “bottom up” evolution of the convection within the equatorial belt and the distinctive “swallowtail shape” of the rain areas, which widen and split toward the west, and it shows how these

features relate to the patterns of boundary layer and free-tropospheric convergence in the vicinity of the rain areas. Shallow, frictionally driven meridional circulation cells to the east and to the west of the rain areas account for the equatorial boundary layer convergence to the east of the rain areas and the divergence to the west of them. Equatorward flow in the Rossby waves to the west of the rain areas also plays a role and a third contributing factor is the fact that the equatorial westerlies to the west of the rain areas are narrower than the easterlies to the east of the rain areas. That all three of these features are present in the Matsuno–Gill solutions for the steady-state response to an equatorial heat source in a shallow-water wave equation model supports the notion that equatorial Kelvin and Rossby waves are the building blocks of the observed lower-tropospheric signature of the MJO.

Besides documenting the three-dimensional structure of the MJO, the results presented in AW1 and AW2 provide a concise summary of the energetics. That the zonal overturning in the meridional plane is predominantly thermally direct is evidenced by the prevalence of downgradient zonal flow in the equatorial plane in Fig. 9 in AW1 and the rising of warm air and sinking of cold air in overturning circulation in the equatorial

plane in Fig. 4 of AW2. The coincidence of westerlies and equatorward flow to the east of the reference longitude and easterlies and poleward flow to the west of it in the meridional cross sections shown in Fig. 3 of AW2 is indicative of an equatorward flux of westerly momentum into the equatorial belt at upper-tropospheric levels and a poleward flux of wave activity, which presumably maintains the flanking Rossby waves against frictional dissipation.

In the Gill (1980) solution for the steady-state response to an isolated equatorial heat source, the Kelvin wave response lies to the east of the heat source and the Rossby wave response to the west of it. In contrast, in Matsuno's solution for the steady-state response to a sinusoidally varying equatorial heat source, the Rossby waves are as prominent to the east of the heat source as they are to the west of it. The patterns in our warm pool composites can be viewed as the response to a strong, concentrated anomalous planetary-scale heat source propagating eastward across the warm pool and a more diffuse, more rapidly propagating, planetary-scale heat sink in the opposing (cool) sector of the tropics, as documented in Fig. 2 of AW1. The observed patterns can thus be viewed as a compromise between (or hybrid of) the Matsuno and Gill solutions. As in the Matsuno solution, a Rossby wave signature is evident both to the west and to the east of the heat source, as evidenced by the poleward meridional wind components in Figs. 3, 7, 9, and 10.

The dipole heat source observed in phase with PC2 of  $\Delta\chi$ —longitudinally shifted so that the heat source in the dipole lies on the reference longitude—also contributes to the Rossby wave response to the east of the reference longitude in our warm pool composites. We have verified that the linear response to a dipole heat source is virtually identical to the superposition of the solutions for the Gill response to a monopole heat source over the reference longitude and a monopole heat sink to the east of it—a configuration that would also contribute to the observed Rossby wave response to the east of the reference longitude in our warm pool composites. Hence, the observed MJO-related lower-tropospheric wind pattern is at least qualitatively consistent with the Matsuno-Gill solutions.

While it might be tempting to say that the structure and evolution of the vertical velocity field in the MJO can be “explained” in terms of the superposition the divergence fields in equatorial Kelvin and Rossby waves, taking into account the frictionally driven component, it should be acknowledged that the resemblance between the observational results in Figs. 9–11 and the theoretical solutions in Fig. 13 is only qualitative, and the analysis presented in this paper does not include thermodynamic variables related to moisture, which could also play a role

in shaping the vertical velocity field. A preliminary analysis (not presented here) indicates that warm pool composites of terms such as moisture tendency and moisture advection exhibit well defined, informative patterns. In view of the apparent influence of the background flow on the structure of the MJO, it would also be of interest to repeat the analyses in AW1 and this paper using subsets of the data that reflect contrasting polarities of the seasonal cycle and the ENSO cycle.

**Acknowledgments.** We thank Chidong Zhang and Daehyun Kim for their time and enlightening discussions on the subject. We appreciate the suggestions and comments from George Kiladis and two anonymous reviewers. We would also like to thank Beth Tully for assistance with the graphics. The first author would like to thank Natalia Hryniw for help in developing Fig. 13. This research was supported by the National Science Foundation's Graduate Research Fellowship Program (NSF-GRFP) Grant DGE-0718124 and by the NSF Grant ATM 1122989.

## APPENDIX

### A Further Look at the Temperature, Vertical Velocity, and Divergence Fields in the MJO Cycle

Figure A1 shows a five-panel sequence of  $\omega$  (left column) and  $\rho \times \text{Div}$  (right column) superposed on  $T$  (contours). The MJO-related  $T$  anomalies can be classified into three regimes: 1) eastward- and downward-propagating waves in the tropical tropopause transition layer (TTL) extending from  $\sim 200$  hPa upward into the lower stratosphere, 2) a layer of midtropospheric anomalies centered  $\sim 250$  hPa, and 3) weaker, upward-propagating anomalies at lower-tropospheric levels. The MJO-related perturbations in vertical velocity exhibit a coherent, eastward-propagating signal, with peak amplitudes of  $\sim 10$  hPa day $^{-1}$  per standard deviation of our indices at the 400-hPa level. Like the  $T$  perturbations, the  $\omega$  perturbations tilt westward with height in the lower troposphere and eastward with height in the TTL. The vertical tilts are much more pronounced in the  $\rho \times \text{Div}$  field shown in the right panels of Fig. A1.

The downward-propagating  $T$  perturbations in the TTL range up to  $0.5^\circ\text{C}$  in peak-to-peak amplitude per standard deviation of our indices. These are the features that are not fully captured by the modal decomposition of the  $u$  and  $Z$  fields in Figs. 5 and 9 of AW1. It is shown in Virts and Wallace (2014) that these equatorial TTL  $T$  perturbations are accompanied by in-phase perturbations in ozone and out-of-phase perturbations in relative

humidity, carbon monoxide mixing ratio, and the areal coverage of thin cirrus clouds. They occur out of phase with downward-propagating perturbations in  $\rho \times \text{Div}$  (Fig. A1, right panels); that is, the flow at 200 hPa and above tends to be divergent in anomalously cold layers and vice versa. Since they extend far above the level of the tops of most of the convective clouds, it is likely that these downward-propagating  $T$  anomalies are induced by planetary-scale vertical velocity perturbations (Kiladis et al. 2005). The most prominent of these downward-propagating features is the cold anomaly over the Indian Ocean in the top panel, which tilts eastward with height, and propagates halfway around the globe in this five-panel sequence. These features are suggestive of a downward-propagating Kelvin wave. It can be inferred from the hypsometric equation and the two-dimensional ( $x, z$ ) continuity equation that the out-of-phase relationship between  $T$  and  $\text{Div}$  in and above the TTL requires an in-phase relationship between  $u$  and  $Z$  [e.g., as in Fig. 7 of Wallace and Kousky (1968)], as observed in Kelvin waves forced from below. In agreement with results of Ryu et al. (2008) and Ryu and Lee (2010), the most prominent of these features is situated directly above the centers of enhanced-suppressed convection.

The  $T$  anomalies in the midtropospheric regime, which range up to a few tenths of a degree Celsius in zero-to-peak amplitude per standard deviation of our indices, are related, through the hypsometric equation, to the  $Z$  anomalies in baroclinic modal structure shown in Fig. 5 of AW1. The longitudinal sector that experiences enhanced rainfall, indicated by the upward vertical velocities (blue shading) in Fig. A1, lies at the western end of the anomalously warm sector in the midtropospheric temperature field so that at a given longitude the cooling that accompanies the passage of the episode of enhanced convection does not occur until near the end of it.

The lower-tropospheric  $T$  and  $\rho \times \text{Div}$  anomalies shown in the right panels of Fig. A1 tilt westward with height such that at a given longitude, features in the  $T$  and  $\rho \times \text{Div}$  profiles are observed first at Earth's surface and deepen with time. In agreement with results of Sperber (2003) and Myers and Waliser (2003), the westward tilt of the  $\omega$  and  $\rho \times \text{Div}$  fields with height becomes more pronounced as the MJO-related disturbances propagate eastward from the Indian Ocean, across the Maritime Continent, and into the western Pacific.

Figure A2 shows sequences of regression maps in which the data for individual levels are weighted in accordance with the PCs shown in Fig. 6. These sequences span the same half MJO cycle as Figs. 2 and A1. In all three columns,  $T_1$  is represented by contours and is scaled to the 250-hPa level as in Fig. 7. Superimposed

upon the  $T_1$  patterns in Fig. A2 are the geographical distributions of the amplitude of the MJO-related OLR (left panels),  $\omega_1$  (middle panels), and  $\omega_2$  (right panels) perturbations, as inferred from linear regression on linear combinations of PC1 and PC2 of  $\Delta\chi$ . The horizontal maps of  $\omega_1$  and  $\omega_2$  are scaled to their corresponding PC values at the 300-hPa level (see Fig. 6). The forward bowing of the patch of ascending motion (negative  $\omega_1$ ) is closely associated with the eastward propagation of positive equatorial  $T_1$  anomalies across the Maritime Continent in Figs. A2a and A2b. As the negative  $T_1$  anomalies develop over the Indian Ocean and propagate eastward (Figs. A2c–e), a region of descent develops and replaces the region of anomalous ascent to the western end of the region of active convection. Thus, the “swallowtail” shape observed in  $\omega_1$  appears to be related to the eastward-propagating Kelvin wave signature in  $T_1$ . The  $\omega_2$  patterns (right panels) exhibit a strong spatial correlation with  $T_1$ , zonally stretching as the  $T_1$  anomalies also stretches zonally from Figs. A2c to A2e. This relationship is apparent not only in the equatorial belt but also in the outer tropics (10°–20°N/S). The  $\omega_2$  extrema are displaced slightly to the east of the  $T_1$  extrema. Regions of ascent are also seen  $\sim$ 30°N/S in association with the flanking Rossby waves.

#### *Characteristics of the decomposed $\omega$ field*

Linear combinations of  $\omega_1$  and  $\omega_2$  can represent the essential features of the evolution of the vertical velocity field during the MJO cycle. The five-panel sequence of vertical profiles depicted in Fig. A3, which represents five different linear combinations of  $\omega_1$  and  $\omega_2$ , can be matched with the sequence of cross sections shown in the right column of Fig. 2. As suggested by this five-panel sequence, ascent over the Maritime Continent, indicated in Fig. A3 by negative values in the  $\omega$  profiles, begins around the time of the minimum of PC2 of  $\Delta\chi$ , as indicated in the left panel ( $\omega_1 \sim 0$ ;  $\omega_2$  at its positive peak  $\sim$ 300 hPa). At this time the vertical velocity profile is indicative of shallow convection, with ascent from the surface up to 600 hPa, and subsidence above that level. As the region of enhanced convection propagates eastward across the Indian Ocean, the layer of ascent over the Maritime Continent deepens, as indicated in the second panel in the right column of Fig. 2. One-eighth MJO cycle later, as the peak rainfall is passing over the Maritime Continent, the profile is evolving in a manner suggestive of a transition from convective cells to stratiform convection with an elevated base. These results are consistent with studies by Kikuchi and Tachibana (2004), Kiladis et al. (2005), Morita et al. (2006), and Benedict and Randall (2007). The evolution of the vertical velocity profile over the Maritime

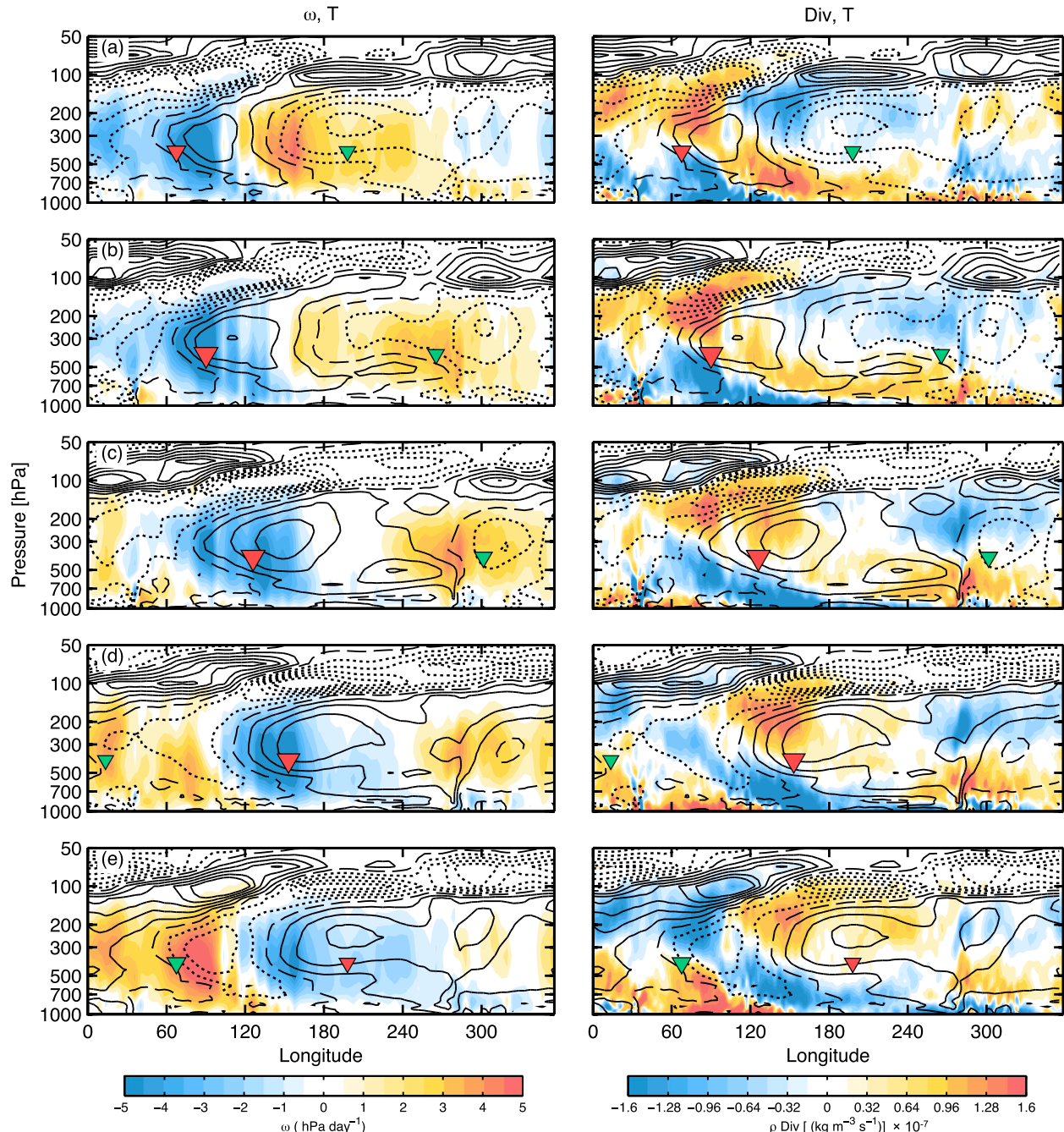


FIG. A1. Longitude–height cross sections of temperature (contours) with (left) vertical velocity (shaded) and (right) mass divergence (shaded), averaged from  $10^{\circ}\text{S}$  to  $10^{\circ}\text{N}$ . Solid contours denote warm anomalies and dashed contours denote cold anomalies. Contour interval is  $0.05^{\circ}\text{C}$ . The zero value of  $T$  is depicted as a dashed contour. The red and green triangles indicate  $\Delta\chi$  maxima and minima, respectively, and are sized in accordance with the amplitude of the  $\Delta\chi$  maximum and minimum. Panels are arranged as in Fig. 2.

Continent that occurs in association with the intra-seasonal MJO cycle is thus analogous to that in the life cycle of individual convective cells in mesoscale convective systems and other equatorial wave modes (Houze 1982; Straub and Kiladis 2003; Mapes et al.

2006; Zuluaga and Houze 2013). While it is not shown,  $\omega_1$  and  $\omega_2$  describe most of the variability associated with equatorial vertical motion ( $10^{\circ}\text{N/S}$ ) and the superposition of both modes replicates the observed vertical velocity field shown in Fig. 4.

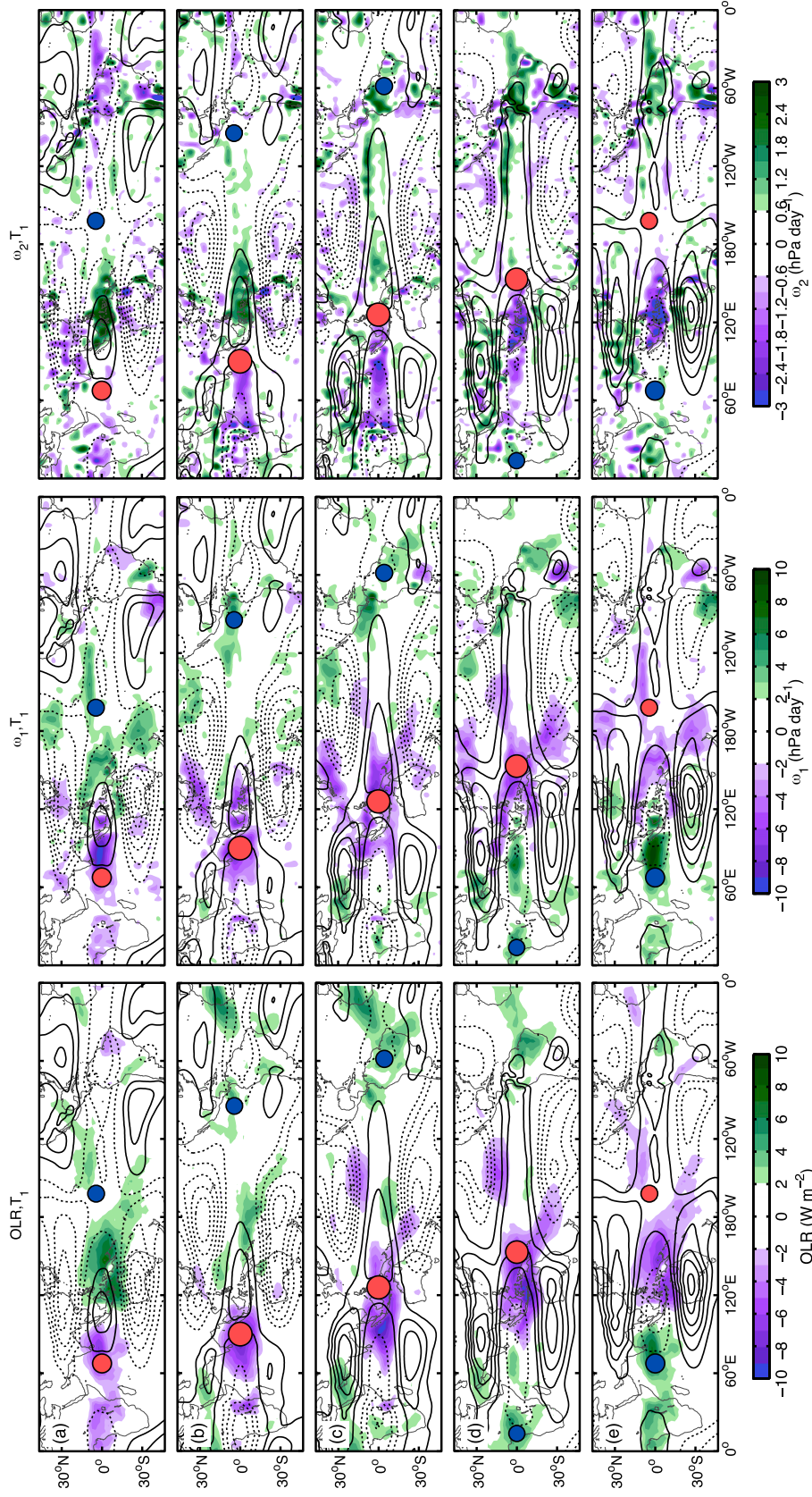


FIG. A2. The temperature  $T_1$  (contours) superimposed upon (left) OLR, (middle)  $\omega_1$ , and (right)  $\omega_2$  anomalies (shaded), regressed on linear combinations of daily values of PC1 and PC2 of  $\Delta\chi$ . Contour interval is  $0.05^\circ\text{C}$ . The  $T_1$  is scaled to the 250-hPa level;  $\omega_1$  and  $\omega_2$  are scaled to the 300-hPa level. Negative values of the scaled  $\omega_1$  are indicative of ascent and positive values of the scaled  $\omega_2$  (green shading) are indicative of shallow convection. Panels are arranged as in Fig. A1. The red and blue circles indicate  $\Delta\chi$  maxima and minima, respectively, and are sized according with the amplitude of the  $\Delta\chi$  maximum and minimum.

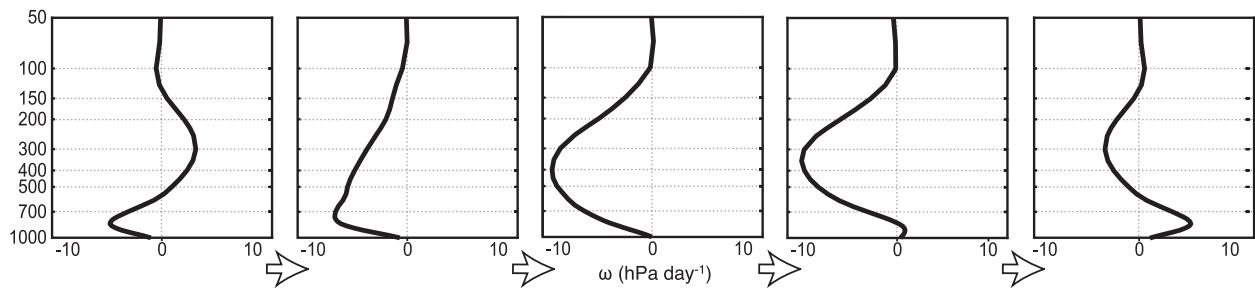


FIG. A3. Representation of the MJO vertical profiles of  $\omega$  belonging to successive octants in the MJO cycle. (left to right) The profiles shown correspond to  $-\omega_2$ ,  $(\omega_2 - \omega_1)/2^{1/2}$ ,  $\omega_1$ ,  $(\omega_2 + \omega_1)/2^{1/2}$ , and  $\omega_2$ . The arrows indicate the sense of the evolution. Vertical velocity is in units of hPa day $^{-1}$ .

## REFERENCES

- Adames, Á. F., and J. M. Wallace, 2014: Three-dimensional structure and evolution of the MJO and its relation to the mean flow. *J. Atmos. Sci.*, **71**, 2007–2026, doi:[10.1175/JAS-D-13-0254.1](https://doi.org/10.1175/JAS-D-13-0254.1).
- , J. Patoux, and R. C. Foster, 2014: The contribution of extratropical waves to the MJO wind field. *J. Atmos. Sci.*, **71**, 155–176, doi:[10.1175/JAS-D-13-0841.1](https://doi.org/10.1175/JAS-D-13-0841.1).
- Bao, M., and D. L. Hartmann, 2014: The response to MJO-like forcing in a nonlinear shallow-water model. *Geophys. Res. Lett.*, **41**, 1322–1328, doi:[10.1002/2013GL057683](https://doi.org/10.1002/2013GL057683).
- Barlow, M., M. Wheeler, B. Lyon, and H. Cullen, 2005: Modulation of daily precipitation over Southwest Asia by the Madden-Julian oscillation. *Mon. Wea. Rev.*, **133**, 3579–3594, doi:[10.1175/MWR3026.1](https://doi.org/10.1175/MWR3026.1).
- Barnes, H. C., and R. A. Houze, 2013: The precipitating cloud population of the Madden-Julian oscillation over the Indian and west Pacific Oceans. *J. Geophys. Res. Atmos.*, **118**, 6996–7023, doi:[10.1002/jgrd.50375](https://doi.org/10.1002/jgrd.50375).
- Benedict, J. J., and D. A. Randall, 2007: Observed characteristics of the MJO relative to maximum rainfall. *J. Atmos. Sci.*, **64**, 2332–2354, doi:[10.1175/JAS3968.1](https://doi.org/10.1175/JAS3968.1).
- Dee, D. P., and Coauthors, 2011: The ERA-Interim reanalysis: Configuration and performance of the data assimilation system. *Quart. J. Roy. Meteor. Soc.*, **137**, 553–597, doi:[10.1002/qj.828](https://doi.org/10.1002/qj.828).
- Deser, C., 1993: Diagnosis of the surface momentum balance over the tropical Pacific Ocean. *J. Climate*, **6**, 64–74, doi:[10.1175/1520-0442\(1993\)006<0064:DOTSMB>2.0.CO;2](https://doi.org/10.1175/1520-0442(1993)006<0064:DOTSMB>2.0.CO;2).
- Gill, A. E., 1980: Some simple solutions for heat-induced tropical circulation. *Quart. J. Roy. Meteor. Soc.*, **106**, 447–462, doi:[10.1002/qj.49710644905](https://doi.org/10.1002/qj.49710644905).
- Haertel, P. T., G. N. Kiladis, A. Denno, and T. M. Rickenbach, 2008: Vertical-mode decompositions of 2-day waves and the Madden-Julian oscillation. *J. Atmos. Sci.*, **65**, 813–833, doi:[10.1175/2007JAS2314.1](https://doi.org/10.1175/2007JAS2314.1).
- Hendon, H. H., and M. L. Salby, 1994: The life cycle of the Madden-Julian oscillation. *J. Atmos. Sci.*, **51**, 2225–2237, doi:[10.1175/1520-0469\(1994\)051<2225:TLCOTM>2.0.CO;2](https://doi.org/10.1175/1520-0469(1994)051<2225:TLCOTM>2.0.CO;2).
- Hoell, A., M. Barlow, and R. Saini, 2012: The leading pattern of intraseasonal and interannual Indian Ocean precipitation variability and its relationship with Asian circulation during the boreal cold season. *J. Climate*, **25**, 7509–7526, doi:[10.1175/JCLI-D-11-00572.1](https://doi.org/10.1175/JCLI-D-11-00572.1).
- Holloway, C. E., and J. D. Neelin, 2007: The convective cold top and quasi equilibrium. *J. Atmos. Sci.*, **64**, 1467–1487, doi:[10.1175/JAS3907.1](https://doi.org/10.1175/JAS3907.1).
- Holton, J. R., 2004: *An Introduction to Dynamic Meteorology*. 4th ed. Academic Press, 535 pp.
- Houze, R. A., Jr., 1982: Cloud clusters and large-scale vertical motions in the tropics. *J. Meteor. Soc. Japan Ser. II*, **60** (1), 396–410.
- , 1989: Observed structure of mesoscale convective systems and implications for large-scale heating. *Quart. J. Roy. Meteor. Soc.*, **115**, 425–461, doi:[10.1002/qj.49711548702](https://doi.org/10.1002/qj.49711548702).
- Hsu, P.-C., and T. Li, 2012: Role of the boundary layer moisture asymmetry in causing the eastward propagation of the Madden-Julian oscillation. *J. Climate*, **25**, 4914–4931, doi:[10.1175/JCLI-D-11-00310.1](https://doi.org/10.1175/JCLI-D-11-00310.1).
- Johnson, R. H., T. M. Rickenbach, S. A. Rutledge, P. E. Ciesielski, and W. H. Schubert, 1999: Trimodal characteristics of tropical convection. *J. Climate*, **12**, 2397–2418, doi:[10.1175/1520-0442\(1999\)012<2397:TCOTC>2.0.CO;2](https://doi.org/10.1175/1520-0442(1999)012<2397:TCOTC>2.0.CO;2).
- Katsumata, M., R. H. Johnson, and P. E. Ciesielski, 2009: Observed synoptic-scale variability during the developing phase of an ISO over the Indian Ocean during MISMO. *J. Atmos. Sci.*, **66**, 3434–3448, doi:[10.1175/2009JAS3003.1](https://doi.org/10.1175/2009JAS3003.1).
- Kikuchi, K., and Y. N. Takayabu, 2004: The development of organized convection associated with the MJO during TOGA COARE IOP: Trimodal characteristics. *Geophys. Res. Lett.*, **31**, L10101, doi:[10.1029/2004GL019601](https://doi.org/10.1029/2004GL019601).
- Kiladis, G. N., K. H. Straub, and P. T. Haertel, 2005: Zonal and vertical structure of the Madden-Julian oscillation. *J. Atmos. Sci.*, **62**, 2790–2809, doi:[10.1175/JAS3520.1](https://doi.org/10.1175/JAS3520.1).
- Kraucunas, I., and D. L. Hartmann, 2007: Tropical stationary waves in a nonlinear shallow-water model with realistic basic states. *J. Atmos. Sci.*, **64**, 2540–2557, doi:[10.1175/JAS3920.1](https://doi.org/10.1175/JAS3920.1).
- Lau, K.-M., and H.-T. Wu, 2010: Characteristics of precipitation, cloud, and latent heating associated with the Madden-Julian oscillation. *J. Climate*, **23**, 504–518, doi:[10.1175/2009JCLI2920.1](https://doi.org/10.1175/2009JCLI2920.1).
- Lau, N.-C., I. M. Held, and J. D. Neelin, 1988: The Madden-Julian oscillation in an idealized general circulation model. *J. Atmos. Sci.*, **45**, 3810–3832, doi:[10.1175/1520-0469\(1988\)045<3810:TMJOIA>2.0.CO;2](https://doi.org/10.1175/1520-0469(1988)045<3810:TMJOIA>2.0.CO;2).
- Li, T., and B. Wang, 1994: A thermodynamic equilibrium climate model for monthly mean surface winds and precipitation over the tropical Pacific. *J. Atmos. Sci.*, **51**, 1372–1385, doi:[10.1175/1520-0469\(1994\)051<1372:ATECMF>2.0.CO;2](https://doi.org/10.1175/1520-0469(1994)051<1372:ATECMF>2.0.CO;2).
- Liebmann, B., and C. A. Smith, 1996: Description of a complete (interpolated) outgoing longwave radiation dataset. *Bull. Amer. Meteor. Soc.*, **77**, 1275–1277.
- Lo, F., and H. H. Hendon, 2000: Empirical extended-range prediction of the Madden-Julian oscillation. *Mon. Wea. Rev.*, **128**, 2528–2543, doi:[10.1175/1520-0493\(2000\)128<2528:EERPOT>2.0.CO;2](https://doi.org/10.1175/1520-0493(2000)128<2528:EERPOT>2.0.CO;2).
- Madden, R. A., and P. R. Julian, 1972: Description of global scale circulation cells in the tropics with a 40–50 day period. *J. Atmos.*

- Sci.*, **29**, 1109–1123, doi:[10.1175/1520-0469\(1972\)029<1109:DOGSCC>2.0.CO;2](https://doi.org/10.1175/1520-0469(1972)029<1109:DOGSCC>2.0.CO;2).
- Maloney, E. D., and D. L. Hartmann, 1998: Frictional moisture convergence in a composite life cycle of the Madden-Julian oscillation. *J. Climate*, **11**, 2387–2403, doi:[10.1175/1520-0442\(1998\)011<2387:FMCIAC>2.0.CO;2](https://doi.org/10.1175/1520-0442(1998)011<2387:FMCIAC>2.0.CO;2).
- Mapes, B., S. Tulich, J. Lin, and P. Zuidema, 2006: The mesoscale convection life cycle: Building block or prototype for large-scale tropical waves? *Dyn. Atmos. Oceans*, **42** (1–4), 3–29, doi:[10.1016/j.dynatmoce.2006.03.003](https://doi.org/10.1016/j.dynatmoce.2006.03.003).
- Matsuno, T., 1966: Quasi-geostrophic motions in the equatorial area. *J. Meteor. Soc. Japan*, **44**, 25–43.
- Morita, J., Y. N. Takayabu, S. Shige, and Y. Kodama, 2006: Analysis of rainfall characteristics of the Madden-Julian oscillation using TRMM satellite data. *Dyn. Atmos. Oceans*, **42** (1–4), 107–126, doi:[10.1016/j.dynatmoce.2006.02.002](https://doi.org/10.1016/j.dynatmoce.2006.02.002).
- Moskowitz, B. M., and C. S. Bretherton, 2000: An analysis of frictional feedback on a moist equatorial Kelvin mode. *J. Atmos. Sci.*, **57**, 2188–2206, doi:[10.1175/1520-0469\(2000\)057<2188:AAOFOO>2.0.CO;2](https://doi.org/10.1175/1520-0469(2000)057<2188:AAOFOO>2.0.CO;2).
- Myers, D. S., and D. E. Waliser, 2003: Three-dimensional water vapor and cloud variations associated with the Madden-Julian oscillation during Northern Hemisphere winter. *J. Climate*, **16**, 929–950, doi:[10.1175/1520-0442\(2003\)016<0929:TDWVAC>2.0.CO;2](https://doi.org/10.1175/1520-0442(2003)016<0929:TDWVAC>2.0.CO;2).
- Powell, S. W., and R. A. Houze, 2013: The cloud population and onset of the Madden-Julian Oscillation over the Indian Ocean during DYNAMO-AMIE. *J. Geophys. Res.*, **118**, 11 979–11 995, doi:[10.1002/2013JD020421](https://doi.org/10.1002/2013JD020421).
- Riley, E. M., B. E. Mapes, and S. N. Tulich, 2011: Clouds associated with the Madden-Julian oscillation: A new perspective from CloudSat. *J. Atmos. Sci.*, **68**, 3032–3051, doi:[10.1175/JAS-D-11-030.1](https://doi.org/10.1175/JAS-D-11-030.1).
- Ryu, J.-H., and S. Lee, 2010: Effect of tropical waves on the tropical tropopause transition layer upwelling. *J. Atmos. Sci.*, **67**, 3130–3148, doi:[10.1175/2010JAS3434.1](https://doi.org/10.1175/2010JAS3434.1).
- , —, and S.-W. Son, 2008: Vertically propagating Kelvin waves and tropical tropopause variability. *J. Atmos. Sci.*, **65**, 1817–1837, doi:[10.1175/2007JAS2466.1](https://doi.org/10.1175/2007JAS2466.1).
- Schumacher, C., R. A. Houze Jr., and I. Kraucunas, 2004: The tropical dynamical response to latent heating estimates derived from the TRMM precipitation radar. *J. Atmos. Sci.*, **61**, 1341–1358, doi:[10.1175/1520-0469\(2004\)061<1341:TTDRTL>2.0.CO;2](https://doi.org/10.1175/1520-0469(2004)061<1341:TTDRTL>2.0.CO;2).
- Sperber, K. R., 2003: Propagation and the vertical structure of the Madden-Julian oscillation. *Mon. Wea. Rev.*, **131**, 3018–3037, doi:[10.1175/1520-0493\(2003\)131<3018:PATVSO>2.0.CO;2](https://doi.org/10.1175/1520-0493(2003)131<3018:PATVSO>2.0.CO;2).
- Stevens, B., J. Duan, J. C. McWilliams, M. Münnich, and J. D. Neelin, 2002: Entrainment, Rayleigh friction, and boundary layer winds over the tropical Pacific. *J. Climate*, **15**, 30–44, doi:[10.1175/1520-0442\(2002\)015<0030:ERFABL>2.0.CO;2](https://doi.org/10.1175/1520-0442(2002)015<0030:ERFABL>2.0.CO;2).
- Straub, K. H., and G. N. Kiladis, 2003: The observed structure of convectively coupled Kelvin waves: Comparison with simple models of coupled wave instability. *J. Atmos. Sci.*, **60**, 1655–1668, doi:[10.1175/1520-0469\(2003\)060<1655:TOSOCC>2.0.CO;2](https://doi.org/10.1175/1520-0469(2003)060<1655:TOSOCC>2.0.CO;2).
- Tian, B., D. E. Waliser, E. J. Fetzer, and Y. L. Yung, 2010: Vertical moist thermodynamic structure of the Madden-Julian oscillation in Atmospheric Infrared Sounder retrievals: An update and a comparison to ECMWF Interim Re-Analysis. *Mon. Wea. Rev.*, **138**, 4576–4582, doi:[10.1175/2010MWR3486.1](https://doi.org/10.1175/2010MWR3486.1).
- Virts, K. S., and J. M. Wallace, 2014: Observations of temperature, wind, cirrus, and trace gases in the tropical tropopause transition layer during the MJO. *J. Atmos. Sci.*, **71**, 1143–1157, doi:[10.1175/JAS-D-13-0178.1](https://doi.org/10.1175/JAS-D-13-0178.1).
- Wallace, J. M., and V. E. Kousky, 1968: Observational evidence of Kelvin Waves in the tropical stratosphere. *J. Atmos. Sci.*, **25**, 900–907, doi:[10.1175/1520-0469\(1968\)025<0900:OEOKWI>2.0.CO;2](https://doi.org/10.1175/1520-0469(1968)025<0900:OEOKWI>2.0.CO;2).
- Wang, B., 1988: Dynamics of tropical low-frequency waves: An analysis of the moist Kelvin wave. *J. Atmos. Sci.*, **45**, 2051–2065, doi:[10.1175/1520-0469\(1988\)045<2051:DOTLFW>2.0.CO;2](https://doi.org/10.1175/1520-0469(1988)045<2051:DOTLFW>2.0.CO;2).
- , and H. Rui, 1990: Dynamics of the coupled moist Kelvin-Rossby wave on an equatorial  $\beta$ -plane. *J. Atmos. Sci.*, **47**, 397–413, doi:[10.1175/1520-0469\(1990\)047<0397:DOTCMK>2.0.CO;2](https://doi.org/10.1175/1520-0469(1990)047<0397:DOTCMK>2.0.CO;2).
- , and T. Li, 1993: A simple tropical atmosphere model of relevance to short-term climate variations. *J. Atmos. Sci.*, **50**, 260–284, doi:[10.1175/1520-0469\(1993\)050<0260:ASTAMO>2.0.CO;2](https://doi.org/10.1175/1520-0469(1993)050<0260:ASTAMO>2.0.CO;2).
- , and —, 1994: Convective interaction with boundary-layer dynamics in the development of a tropical intra-seasonal system. *J. Atmos. Sci.*, **51**, 1386–1400, doi:[10.1175/1520-0469\(1994\)051<1386:CIWBBLD>2.0.CO;2](https://doi.org/10.1175/1520-0469(1994)051<1386:CIWBBLD>2.0.CO;2).
- Webster, P. J., 1972: Response of the tropical atmosphere to local, steady forcing. *Mon. Wea. Rev.*, **100**, 518–541, doi:[10.1175/1520-0493\(1972\)100<0518:ROTTAT>2.3.CO;2](https://doi.org/10.1175/1520-0493(1972)100<0518:ROTTAT>2.3.CO;2).
- Wheeler, M., G. N. Kiladis, and P. J. Webster, 2000: Large-scale dynamical fields associated with convectively coupled equatorial waves. *J. Atmos. Sci.*, **57**, 613–640, doi:[10.1175/1520-0469\(2000\)057<0613:LSDFAW>2.0.CO;2](https://doi.org/10.1175/1520-0469(2000)057<0613:LSDFAW>2.0.CO;2).
- Yoneyama, K., and Coauthors, 2008: Mismo Field Experiment in the equatorial Indian Ocean. *Bull. Amer. Meteor. Soc.*, **89**, 1889–1903, doi:[10.1175/2008BAMS2519.1](https://doi.org/10.1175/2008BAMS2519.1).
- Zhang, C., and S. M. Hagos, 2009: Bi-modal structure and variability of large-scale diabatic heating in the tropics. *J. Atmos. Sci.*, **66**, 3621–3640, doi:[10.1175/2009JAS3089.1](https://doi.org/10.1175/2009JAS3089.1).
- , and J. Ling, 2012: Potential vorticity of the Madden-Julian oscillation. *J. Atmos. Sci.*, **69**, 65–78, doi:[10.1175/JAS-D-11-081.1](https://doi.org/10.1175/JAS-D-11-081.1).
- Zuluaga, M. D., and R. A. Houze, 2013: Evolution of the population of precipitating convective systems over the equatorial Indian Ocean in active phases of the Madden-Julian oscillation. *J. Atmos. Sci.*, **70**, 2713–2725, doi:[10.1175/JAS-D-12-0311.1](https://doi.org/10.1175/JAS-D-12-0311.1).